

3D NUMERICAL MODELS FOR ALONG-AXIS VARIATIONS IN DIKING AT
MID-OCEAN RIDGES

by

田小川

(Tian, Xiaochuan)

A Thesis

Submitted in Partial Fulfillment of the
Requirements for the Degree of
Master of Science

Major: Geophysics

The University of Memphis

May, 2015

Copyright © 2015 Xiaochuan Tian

All rights reserved

Dedication

I would like to dedicate this thesis to my mother, 田霞 (Tian, Xia). I wouldn't have a chance to experience this wonderful world without her giving birth to me. She rears me up by herself with her great love, optimism and peseverence. Without her guidance and support, I will not become who I am.

I also want to dedicate this thesis toward my major thesis advisor: Professor Eunseo Choi. His mentorship defines what a great advisor is like. Without his guidance, neither this thesis nor my fast personal development during these two years is possible. He has kindled a flame that illuminates the way for my future career as a geodynamic modeler.

Acknowledgements

There is no proper words for me to express my deep gratitude toward my thesis advisor, Professor Eunseo Choi. He has changed my life in a very positive way. From him, I have learned what a great researcher and educator should be like. It is because of his unfailing care and understanding that have given me the courage to persevere, to carry on during the darkest days as an international student far away from home. It is his vivid and interesting lessons that have inspired me so much that I want to devote my career into geodynamic modeling. It is his numerous inspiration and encouragement that has motivated me to work super hard (enjoy at the same time) on the fascinating research questions. It is his altruistic share that has provided me with great chances to learn from great researchers, references, and to attend meetings. It is his patience to guide me through my endless silly questions that has nurished and cultivated my capabilities of being an independent researcher. Blessings from Eunseo, my role model, are countless. I will keep them in mind and try my best to relay the torch.

I would also like to thank members of my thesis committee, Professor Christine Powell and Professor Jer-Ming Chiu, for their guidance and support. Especially I want to thank Dr. Chiu for his sharing and advice on my course term projects and for his patience to answer all my silly questions. In addition, I want to thank Dr. Powell for your warm-hearted encouragement and benevolence during my studies at the Center for Earthquake Research and Information (CERI).

My sincere thanks must also go to the CERI and the University of Memphis (UM). Thanks a lot for providing me this great chance to study here with full tuition and graduate research assistanship. It is this kind support that has made my two-year studies at this great institution possible.

I am also grateful to the courses instructors for many vivid and interesting courses that have stimulated my interests in Geophysics, helped me build up my foundation and expanded my horizon in the field. They are Professor Robert Smalley for “Data Analy-

sis in Geophysics”, Professor Charles Langston for “Global Seismology” and “Inverse Methods in Geophysics”, Professor Mitch Withers for “Signal Processing in Earth Science”, Professor Eunseo Choi for “Global Geophysics” and “Geodynamics”, Professor Christine Powell for “Environmental Geophysics”, Professor Randy Cox for “Art of Earth Science”, Professor Jer-Ming Chiu for “Exploration Seismology”. Thank you so much. Especially, I want to thank Professor Withers for your encouragement and your time and efforts for answering all my questions. I would also like to thank Professor Eric Daub for your delicious homemade cakes provided to our graduate students every Wednesday during the “CERI Discussion”. I am probably the person who ate most of them and enjoyed the most.

Many thanks must also go to my dear classmates and research colleagues, with whom, I have lived, studied and worked with during the two years. Especially, I want to thank Yang Yang for your supportive help and share on several of my term projects. Thank you for being a wonderful roommate. I would also like to thank my best “cubic office mate”, Naeem Khoshnevis, for his best company. We’ve been studied together as the most diligent (long staying) people in CERI (12/7). Thank you for those benevolent and uncountable “how are you”, “good morning”, “good night” as well as many good chats. My sincere thank must also goes to Sabber Ahamed, who have been encouraging me during my darkest days when I lost direction. It is his enthusiastic share and encouragement that have helped me went through the bad days.

Special thanks must also go to CERI staffs. Thank you Chris McGoldrick for many of your kindly help and all the nice chats, from which I have learned many new English words. Thank you Tanya Broadbent and Kathleen Tucker for sending me birthday gifts which makes me feel so warm to be a member of CERI families. Thank Christy Chiu and Jer-Ming Chiu for inviting me for Chineses Spring Festival lunch which helped a lot in soothing my nostalgia for hometown. Thank Gary Patterson for your share and benevolence. Thank Deshone Marshall for constantly helping me out in using CERI’s lab com-

puters.

I also want to sincerely thank Center for Writing and Communication of the UM. Especially, I want to thank Bill Schraufnagel for your very supportive helps on revising my Thesis writing as well as practicing my presentations.

I also want to thank Professor 刘洁 (Liu, Jie) and Professor 张珂 (Zhang, Ke) from Sun Yat-sen University, for kindly sharing your computing resources on Tianhe2 to me. Many thanks must also go to the staffs of Penguin, Stampede and Tianhe2 supercomputer centers, thank you so much for all the technical supports. Especially, I would like to thank the support from National Supercomputer Center in Guangzhou, China, for more than 200k of core-hours.

Special thanks must also go to the lifeguards and staffs of the swimming pool of the UM Recreation Center. Thank you for your work in providing me such a safe and enjoyable workout environments. Thank you for accompanying me almost everyday and making sure my safty during I am swimming. I could not endure all the stresses if without being able to enjoy swimming everyday.

In addition, I also want to express my sincere thank to Professor 成谷 (Cheng, Gu), my undergraduate thesis advisor. Thank you for providing me a chance to start my career as a geophysicist. Thank you for all you guidance and share.

I should never forget my deep gratitude to my middle school Math teacher 冯艳 (Feng, Yan) and high school Math teacher 陈胜方 (Chen, Shengfang) and Physics teacher 吕黎洁 (Lyu, Lijie). It is your great education, inspiration, love and care that have cultivated me into a person, who begin able to appreciate the fascinating science world. Your great efforts and patience in teaching me and answering my silly questions have helped me to build up a good foundation for my future studies as a science student.

Special thank also needs to go to a special person, 张思婉 (Zhang, Siwan). Thank you for planted a seed of love and beauty deeply in my heart that have been encouraging and inspiring me through time.

Finally, I want to thank my families. There simply is no proper word for expressing my gratitude. Thank you so much my dear grandfather 田升恒 (Tian, Shengheng), and grandmother 王德芬 (Wang, Defen), who have reared me up with great love and care. Thank you so much my grandgrandfather 田光宗 (Tian, Guangzong). I will never forget your last words for encouraging me to be a good person and a diligent student.

Thank you my dear mother, 田霞 (Tian, Xia). You are always a great mother to me. Thank you so much for rearing me up by yourself with your great courage, optimism, love and care. Without you, there is no me.

“In the midst of winter, I found there was, within me, an invincible summer.”

—Albert Camus

“People have no higher calling than to strive for the greater good of humankind and society and that the future of humanity can be assured only when there is a balance between scientific development and the enrichment of the human spirit.”

—Kazuo Inamori

“不失其所者久，死而不亡者寿。”

—《道德经》

Abstract

Tian, Xiaochuan. M.S. The University of Memphis. May 2015 Master of Science.
3D Numerical Models for Along-axis Variations in Diking at Mid-Ocean Ridges. Major
Professor: Dr. Eunseo Choi.

Bathymetry of ocean floors reveals a great variety of morphologies at Mid-ocean Ridges (MORs). Previous studies showed that the morphologies at slow spreading MORs are mainly controlled by the ratio between rates of magma supply and plate extension. 2D models for the across-ridge cross-sections have been successful in explaining many of the observed morphological features such as abyssal hills and oceanic core complexes. However, the magma supply varies along the ridge and the interaction between the tectonic plates and magmatism at MORs are inevitably 3D processes. We propose to investigate the consequences of the along-axis variability in diking in terms of faulting pattern and the associated structures. This work will include implementation of an algorithm of parameterizing repeated diking in a 3D parallel geodynamic modeling code.

Table of Contents

Chapter	Page
1 Introduction	1
1.1 Review of Literature	1
1.2 Statement of Research Purpose	5
2 Methods	7
2.1 Method of approach	7
2.2 Model Setup	8
2.3 Parameters to control	9
3 Results	13
3.1 Reference model M28LinT1	13
3.1.1 Constant M model M88ConT2	17
3.2 Main characteristics of the models	18
3.2.1 Location of termination	19
3.2.2 Geometry of trough	20
3.2.3 Inward fault jump	21
3.2.4 Fault alternation	21
3.2.5 Mass wasting	21
3.2.6 Hourglass-shaped median valley	22
3.2.7 Corrugations and mullion structures	24
3.3 Effects of the functional forms of M variation	28
3.3.1 M28(Lin, Sin, Sqrt)T1	28
3.3.2 M58(Lin,Sin,Sqrt)T2	31
3.4 Effects of the weakening rate	32
3.4.1 M57SinT1 versus M57SinT2	32

3.4.2	M58SinT1 versus M58SinT2	35
3.4.3	M58SqrtT1 versus M58SqrtT2	39
3.5	Effects of the range of M variation	41
3.5.1	(M28 M57 M58)SinT1	41
3.5.2	M57SinT2 versus M58SinT2	43
3.5.3	M28LinT1 versus M57LinT1	43
3.5.4	M28SqrtT1 versus M58SqrtT1	44
3.5.5	M57SqrtT2 versus M58SqrtT2	45
4	Discussion	47
4.1	Summary of Results	47
4.2	Fault Alternation	49
4.2.1	Trade-off between bending and weakening	49
4.2.2	Alternating on conjugate plate	51
4.2.3	Secondary near-axis normal fault	51
4.2.4	Effect of along ridge-axis coupling	51
4.3	Corrugations	52
4.3.1	Wavelength of corrugations	52
4.4	Influence of healing	52
4.5	Comparing model results with nature observation	52
4.5.1	Cut back at 13°N Mid-Atlantic Ridge (M28SqrtT1)	52
4.5.2	Double dome at 23°N Mid-Atlantic Ridge (Kane Megamullions) (Several models)	53
4.5.3	Atlantis Massif Shape at 30°N Mid-Atlantic Ridge ()	53
4.5.4	Shear low	53
4.5.5	Corrugations	53
4.6	Model Limitation	53
4.6.1	Fixed thermal structure effects and justification	53

4.7	Recommendation for Future Research	54
5	Conclusions	55
	Bibliography	56

List of Tables

1	Summary of 3D Model Parameters	11
2	List of 3D numerical experiments.	12
3	Average M values of the 20 km segment. (The value is calculated by integrating M along the ridge axis and divided by the length of the model domain in z-axis.)	31
4	Model behaviors in short.	47
5	Linear functional form.	47
6	Sinusoidal functional form.	48
7	Square root functional form.	48

List of Figures

1	Profiles of bathymetry across MORs.	2
2	Two bathymetric profiles across the Mid-Atlantic Ridge around 30°N with vertical exaggeration of 10. A-A' is closer to the segment center while B-B' is at the tip of the segment.	2
3	Relationship between the maximum crustal thickness variations (ΔH_c) along a ridge segment and the segment length (L). The dashed line is the best-fit linear regression of the combined data. [Chen and Lin, 1999]	3
4	Upper one: modeling result for fast spreading agrees well with the observation of East Pacific Rise. Lower one: modeling result for slow spreading ridges agrees well with the bathymetry of Mid Atlantic Ridge. [Buck et al., 2005]	5
5	Snapshots of modeled fault behavior and seafloor morphology for values M = 0, 0.5, and 0.7; model allows thermal evolution. Structural interpretation is superimposed on modeled distribution of strain rate; model time is indicated in panels at lower right; dashed white line at bottom is 600 °C isotherm and approximates the brittle-ductile transition; dashed seafloor is original model seafloor, red seafloor is that formed dominantly by magmatic accretion, and solid bold seafloor is fault surface.[Tucholke et al., 2008, Whitney et al., 2012]	6
6	Essential components of the numerical method.	8
7	Model setup	9
8	Evolution of plastic strain and surface topography of the reference model M28LinT1 (Table 2). Each snapshot shows plastic strain plotted on the model domain and the five times exaggerated topography. Initial seafloor is marked as a reference of 0 km of the topography. The black dashed lines are the terminations of the detachment faults. The red dashed lines in g) and h) are the transfer faults that connect the terminations along the ridge. The inset in f) plots plastic strain with opacity linearly proportional to its value.	13

9	Bird's-eye view of the evolution of breakaway (marked by green bold line) and depressed narrow zone ("trough") along the ridge axis (red dashed line in (a)). This figure share the same color scales with Figure 8.	14
10	Bending stress illustration. The blue line is the neutral plane where $\sigma_{xx} = 0$. Above the neutral plane is compression ($\sigma_{xx} < 0$) and beneath it is tension ($\sigma_{xx} > 0$).	15
11	Bird's-eye view of velocity field with plastic strain plotted with ^{EC:} <u>opacity</u> [why do you need transparency in this figure?] ^{XT:} <u>if not transparent, the velocity vectors will be hidden</u> linearly proportional to its value. (color scale is the same as Figure 8.a))	16
12	Bird's eye view of σ_{xz}	17
13	Evolution of plastic strain and surface topography of the model: M88ConT2 (Table 2). (color scale of topography is the same as Figure 8.a)	18
14	The second invariant of strain rates plotted on the reference model's vertical cross-sections along the ridge at 107.5 kyr. Terminations and breakaways are marked by black and red arrows.	19
15	The weak detachment fault tip reaches the pre-existing shear stress. Plastic strain is plotted with opacity linearly proportional to its value.	21
16	Velocity of the mass wasting hanging wall. Magnitudes of the velocity are shown by the colors of the arrow heads. Plastic strain is plotted with opacity linearly proportional to its value.	22
17	Plastic strain, topography and stresses evolution for M28SqrtT1.	23
18	Along ridge axis σ_{xz} (bird's-eye view of three layers of model domain) (positive(red) means clockwise). Plastic strain is plotted with opacity linearly proportional to its value.	24

19	M28SqrtT1 (Table 2). Bending stress drop (a versus b) at the lower M side due to the cut-back. No bending stress drop (c versus d) at the higher M side as a comparison.	25
20	New fault front chase after cut-back.	25
21	Bird's-eye view of the evolution of the hourglass shape median valley. It is generated by attaching the topography of the M28SqrtT1 model to its mirror reflection by assumming symmetrical M variation (0.2 to 0.8 to 0.2).	26
22	Higher σ_{xx} shows inside the median valley on the negative x -axis direction of the ridge axis.	26
23	Bird's-eye view of the evolution of the corrugations. Color scales for the topography is the same as Figure 8.	27
24	Evolution of mullion structures.	27
25	Three functional forms of M variation. M begins to exceed the M = 0.5 black line at Z=10 km, 7 km, 5 km for M28LinT1, M28SinT1 and M28SqrtT1 respectively.	28
26	Bird's-eye view for comparing the length and timing of inward fault jump. .	29
27	$\partial M / \partial Z$ comparision.	30
28	Bird's-eye view of the topography. (without vertical exaggeration.)	30
29	M57SinT2 versus M57SinT1 (Table 2)	32
30	Faulting and stress evolution for M57SinT1.	33
31	M57SinT2 (Table 2) faulting and stress evolution with respect to time. . . .	34
32	Faulting and stresses evolution (M58SinT1).	35
33	Plastic strain for M58SinT1 at 350 kyr.	36
34	Evolution of faulting and morphologies of M58SinT1.	37
35	Faulting and stresses evolution of M58SinT2.	38
36	M58SqrtT1 (Table 2) faulting and stress evolution with respect to time. . . .	39
37	Faulting and stresses evolution for M58SqrtT2.	41

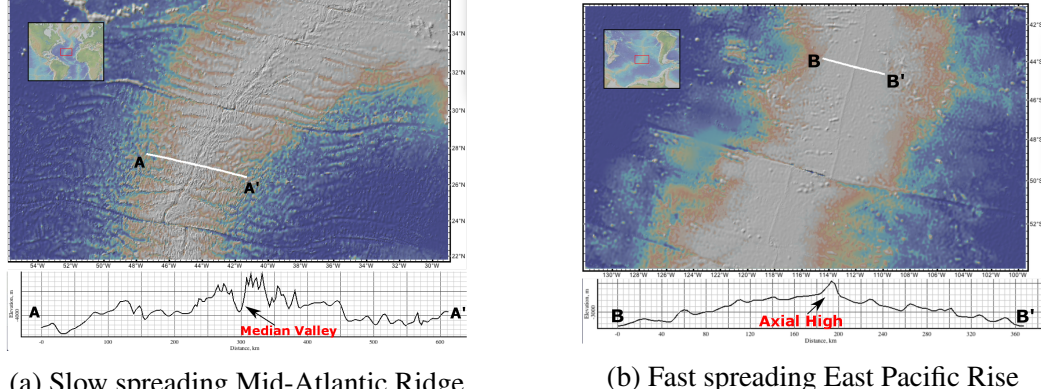
38	M28SinT1 (Table 2) faulting and stress evolution with respect to time.	42
39	M57LinT1 (Table 2) faulting and stress evolution with respect to time.	44
40	M57SqrtT2 (Table 2) faulting and stress evolution with respect to time.	45
41	Trade-off between change in bending force ΔF_b and weakening in the fault interface ΔF_w . H is the thickness of the brittle crust and γ is the size of initial weak perturbation and A defines the maximum bending force change. (For more details, please refer to [Lavier et al., 2000])	49
42	Comparing nature observation at 13°N Mid-Atlantic Ridge to the Cut back behavior of model M28SqrtT1. The model topography is a mirror symmetric flip according to the dash line, it reveals the case of M varies in a square root functional form from 0.2 to 0.8 to 0.2. For discussion on cut back formation mechanism, please refer to Section ?? . The bathymetry is from GeoMapApp [Ryan et al., 2009].	53
43	Comparing nature observation at 13°N Mid-Atlantic Ridge to the Cut back behavior of model M28SqrtT1. The model topography is a mirror symmetric flip according to the dash line, it reveals the case of M varies in a square root functional form from 0.2 to 0.8 to 0.2. For discussion on cut back formation mechanism, please refer to Section ??	54

1 Introduction

Around 70% area of the Earth's crust is the oceanic crust. New oceanic crust is constantly forming at the mid-ocean ridges (MORs), the longest mountain chains on the Earth. Seismic and volcanic activities are frequently happening along the MORs due to incessant seafloor spreading and magma upwelling. The interactions between the tectonics and magmatism along the MORs are considered to be responsible for the variations in the seafloor morphology [Buck et al., 2005; Tucholke et al., 2008]. Geodynamic modeling along with a variety of geological, geophysical observation and lab experiment constraints have been used to study how does the interaction system between tectonics and magmatism at the MORs work under geological time scale [e.g. Tucholke and Lin, 1994; Blackman et al., 2002; Behn et al., 2006; Behn and Ito, 2008; Ito and Behn, 2008; Baines et al., 2008; Escartín et al., 2008; Canales et al., 2008; Dick et al., 2008; Dannowski et al., 2010; Olive et al., 2010; Reston and Ranero, 2011; Reston and McDermott, 2011;].

1.1 Review of Literature

According to [Fowler, 2004], variations in mid-ocean ridge morphologies are mainly controlled by four factors: magma supply, tectonic strain, hydrothermal circulation and spreading rate.^{XT:}Clarify the relationship between the four factors and try to cite the original work for each of them. (in Fowler2004, they didn't mention the ref for these four factors, page417 Chapter9.4.1) Among them, the spreading rate shows the strongest correlation with the ridge morphology. Slow-to-intermediate spreading ridges (half spreading rate less than 4 cm/yr) produce median valleys that are typically 10~20 km wide and 1~2 km deep (e.g., Mid-Atlantic Ridges, Figure 1a). Fast-spreading ridges (half spreading rate greater than 5 cm/yr) like the East Pacific Rise have axial highs that are 10~20 km wide, 0.3~0.5 km high (Figure 1b).



(a) Slow spreading Mid-Atlantic Ridge

(b) Fast spreading East Pacific Rise

Figure 1: Profiles of bathymetry across MORs.

Slow spreading ridges exhibit along-axis variations in off-axis morphology, the width and depth of median valleys and crustal thickness. Figure 2 shows that the topographic profile near to the center of the ridge segment (A-A') is rather symmetric and has higher frequency with a median valley \sim 12 km wide and \sim 1 km deep. In contrast, the near-tip profile (B-B') is asymmetric and has a much lower frequency with a median valley wider than 30 km and shows a greater relief (\sim 3 km). The maximum along-axis variation in crustal thickness ΔH_c is linearly increasing with segment length L [Chen and Lin, 1999] and the relationship is $\Delta H_c(L) = 0.0206L$ (Figure 3).

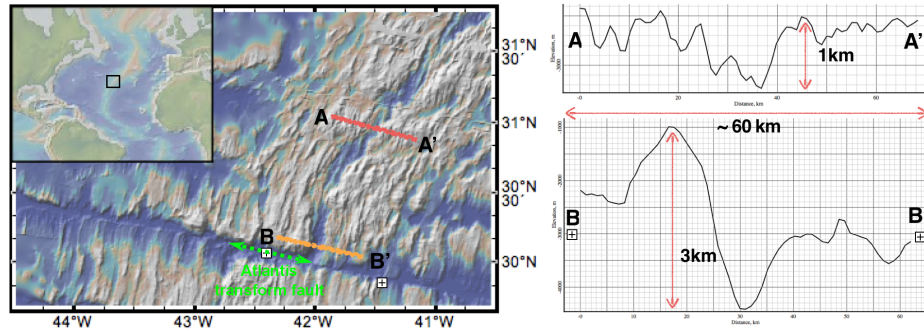


Figure 2: Two bathymetric profiles across the Mid-Atlantic Ridge around 30°N with vertical exaggeration of 10. A-A' is closer to the segment center while B-B' is at the tip of the segment.

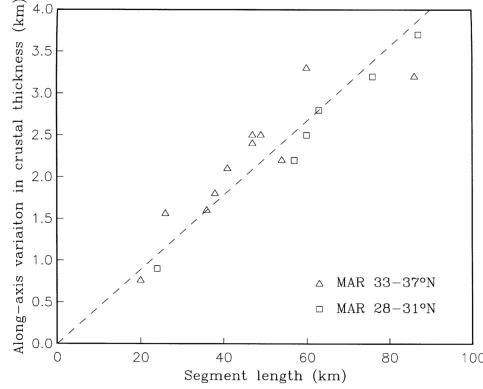


Figure 3: Relationship between the maximum crustal thickness variations (ΔH_c) along a ridge segment and the segment length (L). The dashed line is the best-fit linear regression of the combined data. [Chen and Lin, 1999]

Magma supply at the MORs is mostly a passive process when no hot plume is present [Fowler, 2004]. Driven by both vertical pressure difference and buoyancy due to horizontal density difference, hot mantle rises up to fill the vacated room produced by the plate separation. Since lithostatic pressure decreases with shallower depth in the crust, decompression of the upwelling hot mantle results in partial melting. The generated magma upwells to the upper crust and supplies the diking at the ridge center which releases extensional stresses resulting from the extension forces (e.g slab pull, viscous mantle drag) that drive the seafloor spreading.

The passive nature of the melting processes at the MORs leads to the major difference between fast and slow spreading ridges. At fast spreading ridges, due to much higher spreading rates, vacated room is frequently produced by plates separation. This results in a relatively sufficient magma supply for the frequent diking that can approximately release all the tensional stress generated by plates extension. However, the amount of magma supplied at the slow spreading ridges is restricted by the lower rate of the vacated room being produced by plates separation. Diking can only partially releases the tensional stress under the limited magma supply and thus the oceanic lithosphere experiences internal deformations (e.g. tectonics process like normal faulting) when the accumulated extensional stress exceeds the strength of the crust.

Buck et al. [2005] attributed the contrasting faulting patterns and ocean floor morphology of fast- and slow-spreading ridges to the difference in the amount of diking-accommodated plate extension. They defined the ratio between the rates of diking and plate separation as $M = V_{dx}/2V_x$, where V_{dx} is the rate of opening by diking at a MOR and V_x is the half spreading rate of the MOR. According to this definition, $M = 1$ represents the case where dike injection is so frequent that magma supply is sufficient to release all the tensional stresses from plate separation. $M = 0$ corresponds to the case of no magma supply, in which diking does not account for any of the plate motion and therefore plates kinematics requires plates to go through internal deformations. As shown in Figure 4, an axial high forms at a fast spreading ridge ($M = 1$) due to buoyancy from lateral density difference across ridge axis but a median valley forms at a slow-spreading ridge ($M = 0.5$) due to near-axis normal faulting, which is in turn caused by the stretching of oceanic lithosphere.

Tucholke et al. [2008] expand the investigation on the role of M in the mid-ocean ridge mechanics. They focus on the faulting behaviors of slow spreading ridges and find that the OCCs are most likely to form when M varies from 0.3 to 0.5. When $M = 0.7$ (Fig. 5), repeated diking pushes faults that have formed at the spreading center away from the ridge axis. Since the thickness of the brittle layer increases away from the ridge axis due to cooling effects, frictional and bending energy for maintaining the fault also increases. When the energy needed for maintaining an existing fault exceeds the energy for breaking a new near-axis fault, the old fault is replaced by the new one and most of the extension is accommodated by the new fault. When $M = 0.3 \sim 0.5$, the normal fault remains active for a long time and rotates to a very low angle normal fault (detachment fault), exhuming the lower crust and mantle materials to the seafloor. When $M < 0.3$, most of the tension is accommodated by intra-plate deformations rather than by diking and as a result, faulting pattern is more complicated and unsteady.

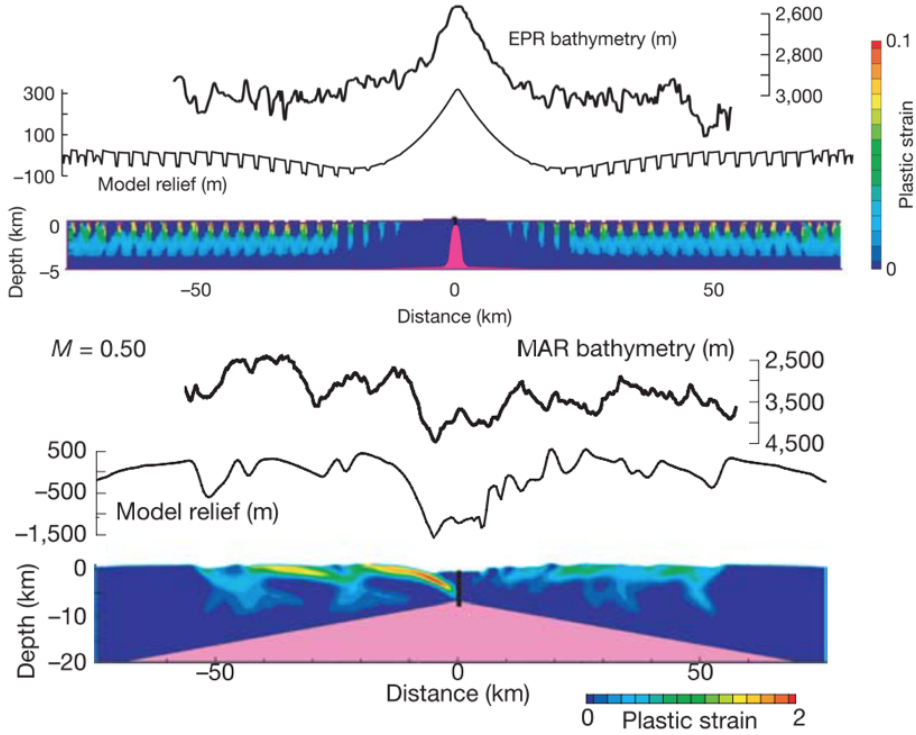


Figure 4: Upper one: modeling result for fast spreading agrees well with the observation of East Pacific Rise. Lower one: modeling result for slow spreading ridges agrees well with the bathymetry of Mid Atlantic Ridge. [Buck et al., 2005]

1.2 Statement of Research Purpose

The M-factor formulation used in the previous 2D models [Tucholke et al., 2008, Buck et al., 2005] successfully explained major features found in across-ridge profiles of seafloor bathymetry. However, 2D models have limitations in studying the along-ridge variations in morphology and faulting patterns. Magma supply at fast spreading ridges seems always sufficient for accommodating plate motions with little variation along the ridge axis. The relatively uniform topography along fast spreading ridges is considered to be consistent with the uniform abundance of the magma supply. However, along the slow spreading ridges, bathymetry, gravity anomaly and results from reflection and refraction seismology show strong correlation with variation in crustal thickness [Ryan et al., 2009, Chen and Lin, 1999, Lin et al., 1990, Tolstoy et al., 1993]. Because oceanic crust is mainly formed by upwelled magma at the ridge, variation in the thickness of the crust implies

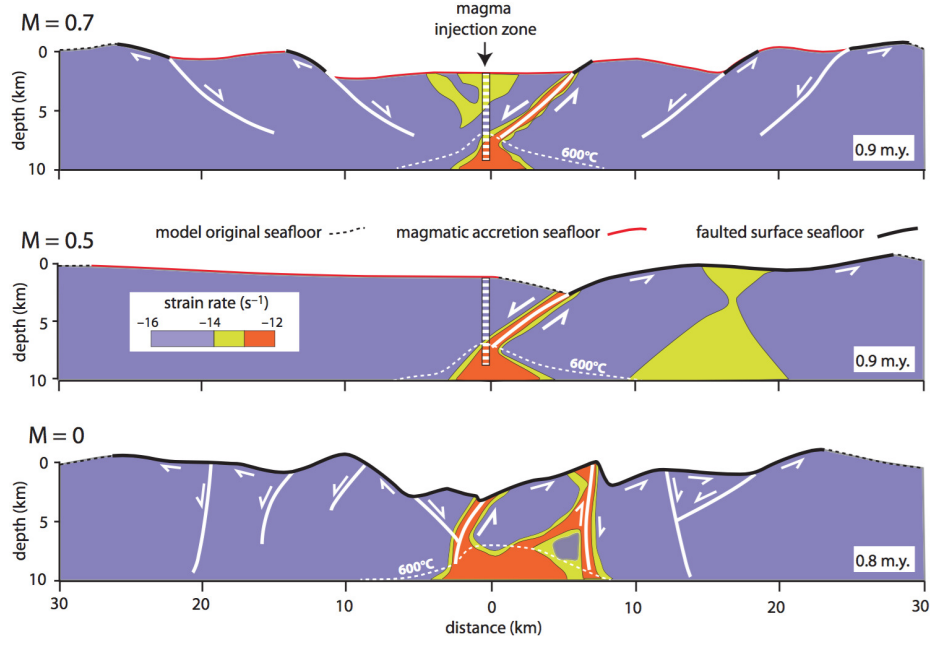


Figure 5: Snapshots of modeled fault behavior and seafloor morphology for values $M = 0, 0.5$, and 0.7 ; model allows thermal evolution. Structural interpretation is superimposed on modeled distribution of strain rate; model time is indicated in panels at lower right; dashed white line at bottom is $600\text{ }^{\circ}\text{C}$ isotherm and approximates the brittle-ductile transition; dashed seafloor is original model seafloor, red seafloor is that formed dominantly by magmatic accretion, and solid bold seafloor is fault surface.[[Tucholke et al., 2008](#), [Whitney et al., 2012](#)]

variation in magma supply. At slow spreading ridges, the degree of cooling by hydrothermal circulation, thermal structures and even local spreading rate [[Baines et al., 2008](#)] also varies both along and across the ridge axis and they appear interrelated. Thus, for slow-to-intermediate spreading ridges, the interactions between tectonics and magmatism at MORs are inevitably 3D processes and 3D numerical models are desirable for better understanding factors controlling both across- and along-ridge topography variations.

The purpose of this thesis is to extend the M -factor formulation originally developed for 2D models to 3D by implementing it into a 3D numerical modeling code SNAC (StGermaiN Analysis of Continua) [[Choi et al., 2008](#)]. By systematically exploring the behaviors of the 3D models and comparing them with observations, we will be able to better understand how the mid-ocean ridge magmatism and tectonic deformations interact.

2 Methods

2.1 Method of approach

The numerical modeling code, SNAC (StGermaiN Analysis of Continua), is an explicit Lagrangian finite element code that solves the force and energy ~~XT: find out which one is energy balance equation~~ balance equations for elasto-visco-plastic materials. Figure 6 shows major components of SNAC.

For each time step, strain and strain rates are updated based on the initial or previous velocity fields under the constraints from boundary conditions. A constitutive model returns updated stresses corresponding to these deformation measures. Internal forces are then calculated from the updated stresses, which is plugged into the momentum balance equation together with the body force term. Then, the damped ~~XT: better understand the damped force~~ net force divided by inertial mass yields acceleration at a node point, which is time-integrated to velocity and displacement.

A 3D domain is discretized into hexahedral elements, each of which is in turn divided into two sets of tetrahedra. This symmetric discretization prevents faulting from favoring a specific direction or “mesh grains”.

Rheology for the oceanic lithosphere is assumed to be elasto-visco-plastic (EVP). When viscosity is high at low temperature, the EVP rheology implemented in SNAC essentially becomes the Mohr-Coulomb plasticity with strain softening that can create shear bands that behave like faults. Strain softening is realized by cohesion decreasing with increasing amount of permanent (i.e., plastic) strain. I assume this relationship is linear for simplicity. It is sufficient for a full description of such a linear strain weakening to define initial and final values of cohesion and a critical plastic strain at which cohesion becomes the final value. I define the rate of strain weakening as the cohesion difference divided by the critical plastic strain and use it as one of the model parameters. When temperature is high and viscosity is low, the rheology becomes the Maxwell viscoelasticity and can

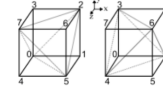
model creeping flow. This property of the EVP model makes it possible to set up a structure with a brittle lithosphere and a ductile asthenosphere through a proper temperature distribution. Rheological parameters are taken from previous studies that use a similar rheology [e.g., [Buck et al., 2005](#); [Tucholke et al., 2008](#)] or from lab experiments [e.g., [Kirby and Kronenberg, 1987](#)].

For 3D diking processs, the strain $\Delta\varepsilon_{xx}$ associated with diking leads to stresses changes, $\Delta\sigma_{xx}$, $\Delta\sigma_{yy}$ and $\Delta\sigma_{zz}$. These stress changes due to diking are computed according to the linear elastic constitutive equations $\sigma_{ij} = \lambda\varepsilon_{kk}\delta_{ij} + 2\mu\varepsilon_{ij}$.

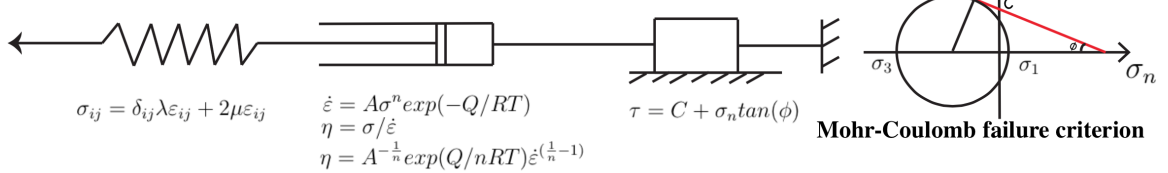
SNAC: a 3D, MPI parallelized, updated Lagrangian explicit finite difference code for modeling long-term tectonic evolution of the Earth's elasto-visco-plastic crust and mantle. (Choi et al., 2008)

$$\text{Momentum Balance Equation: } \frac{\partial\sigma_{ij}}{\partial x_j} + \rho g_i = \rho \frac{Dv_i}{Dt}$$

Spatial Decritization: A 3D domain is discretized into hexahedral elements, each of which is filled with two sets of 5 tetrahedra.



Elasto-Visco-Plastic (EVP) Rheology:



Diking M Formulation: $M = Vdx / 2Vx$ (Vdx is the diking velocity in x direction, 2Vx is the full spreading velocity)

Stresses introduced by a dike accretion strain(dike widening) $\Delta\varepsilon_{xx}$ in each time step dt:

$$\Delta\sigma_{xx} = (\lambda + 2\mu)\Delta\varepsilon_{xx} \quad \Delta\sigma_{yy} = \lambda\Delta\varepsilon_{xx} \quad \Delta\sigma_{zz} = \lambda\Delta\varepsilon_{xx}$$

Figure 6: Essential components of the numerical method.

2.2 Model Setup

The 3D models have a common geometry of $60 \text{ km} \times 20 \text{ km} \times 20 \text{ km}$ in x , y and z axes respectively with a resolution (Δx) of 1 km (i.e., Δx is the size of each hexahedron element). The initial temperature field linearly increases from 0°C at the top surface to 240°C at the depth of 6 km, reflecting enhanced cooling due to hydrothermal circulation (Fig. 7). Below 6 km, the temperature profile follows the semi-infinite half-space cooling model of moving plates [e.g., [Turcotte and Schubert, 2002](#)]. Two sides perpendicular

to the z coordinate axis are free-slip. The top surface has vertical tractions from water columns, of which heights are locally determined as $(4000 - h(x, z))$ m, where $h(x, z)$ is the topography at a location, (x, z) . The bottom surface is supported by the Winkler foundation. Temperature is fixed at 0 °C on the top surface and at 1300 °C on the bottom surface.

Diking, represented by the factor M as described above, is assumed to occur in the middle of the domain (Fig. 7), where the lithosphere is the thinnest.

We adopt the linear isotropic elasticity, power-law viscosity of dry diabase [e.g., Kirby and Kronenberg, 1987, Buck et al., 2005] and the Mohr-Coulomb plastic model. The complete list of model parameters are given in Table 1.

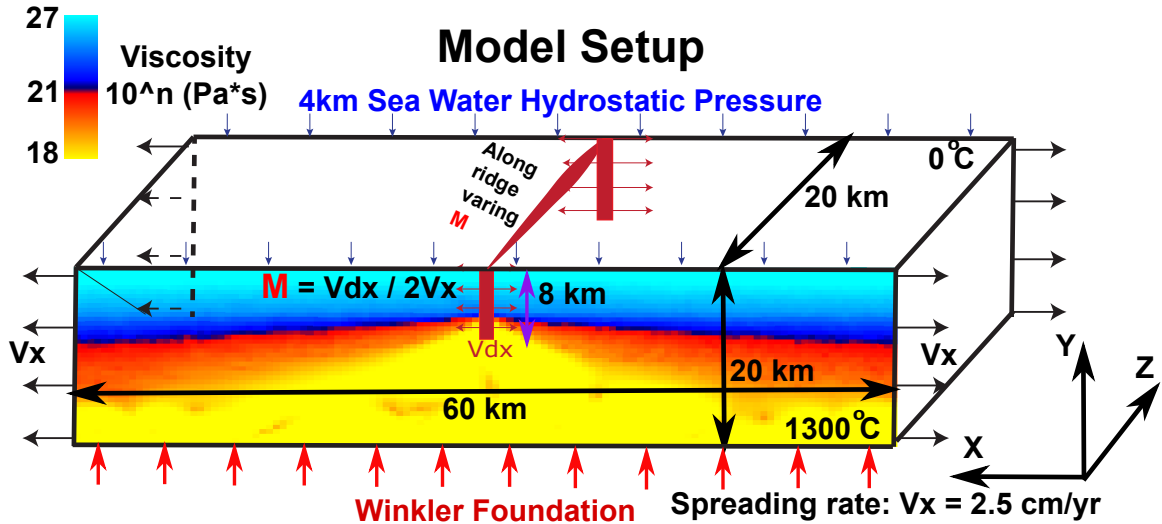


Figure 7: Model setup

2.3 Parameters to control

Before running 3D models, I have run hundreds of pseudo-2D models for initial setup and benchmarking with previous studies [e.g., Buck et al., 2005, Tucholke et al., 2008]. Preliminary pseudo-2D results show that the model behavior in faulting pattern is sensitive to the rate of strain weakening. Two cases of strain weakening are tested in the 3D models. In one case (denoted as Type 1 weakening), cohesion linearly decreases from

44 MPa (denoted as C_i) to 4 MPa (C_e) for plastic strain accumulating from 0 ($\varepsilon_{p_i}^1$) to 0.1 ($\varepsilon_{p_e}^1$). It has a characteristic fault slip of 150 m for pseudo-2D models and 300 m for 3D models. The other case (Type 2 weakening) assumes cohesion linearly decreasing from 44 MPa (C_i) to 4 MPa (C_e) for plastic strain accumulating from 0 ($\varepsilon_{p_i}^2$) to 0.33 ($\varepsilon_{p_e}^2$). In this case, the characteristic fault slip for pseudo-2D models is 500 m and for 3D models is 1 km. The characteristic fault slip is defined as $\Delta X_c = 3\Delta x \varepsilon_{p_e}$ where $3\Delta x$ represents the thickness of the shear bands which is usually 2 to 4 times Δx (size of a hexahedron element) [Lavier et al., 2000]. When ΔX_c amount of slip takes place at the fault interface, the cohesion of the material at the faulting interface decreases to C_e . In this way, under the same amount of ΔX_c , models with different resolution should produce the same faulting patterns.

Meanwhile, although how to estimate the M values from observations is a subject of on-going research, we do have constraints from a large dataset of bathymetry, gravity and seismic surveys as well as geological drilling. Generally, at slow spreading ridges, magma supplies mostly at the center of the ridge segment and decreases towards the tip of the segment [Tolstoy et al., 1993, Chen and Lin, 1999, Carbotte et al., 2015]. There is also evidence for shorter wavelength of 10 to 20 km discrete focus of magma accretion along the ridge axis [Lin et al., 1990].

The numerical cost of a 3D model is non-trivial. For 2 Myr of model time, each model usually runs on 192 cores for about 48 hours (i.e., around 10^4 core-hours). Based on the observational and computational constraints, I start considering a few scenarios of variations in M along the ridge axis. They are 1) three types of functional forms (i.e. linear, sinusoidal and square root); 2) three ranges of M variation along the ridge axis (0.5~0.7 (M57); 0.5~0.8 (M58); 0.2~0.8 (M28)) and 3) two types of weakening rate (type 1 and type 2).

Till now, $11 + 1$ 3D models are run (11 models with M varying along the ridge-axis and 1 model with constant M = 0.8. The complete list of 3D models is given in Table 2.

Table 1: Summary of 3D Model Parameters

Number	Variable	Description	Value	Units
1	W_{dike}	Dike width	2	km
2	D_{dike}	Dike depth	8	km
3	H	Crustal thickness at dike	6	km
4	dT/dy	Crustal thermal gradient	40	K/km
5	T_1	Temperature at lower boundary of crust	240	°C
6	g	Gravity acceleration	10	m/s ²
7	$demf$	Dimensionless force damping factor	0.8	N/A
8	dt	Time step	1.5768e+07	second
9	$topokappa$	Parameter for topography smoothing	0	N/A
10	$shadowDepth$	Ghost elements for parallel computing	2	N/A
11	$meshI$	Mesh number in X direction	60	N/A
12	$meshJ$	Mesh number in Y direction	20	N/A
13	$meshK$	Mesh number in Z direction	20	N/A
14	L_I	Length in X direction	20	km
15	L_J	Length in Y direction	20	km
16	L_K	Length in Z direction	20	km
17	ρ	Density	3000	kg/m ³
18	λ	Lamé's constant	30	Gpa
19	μ	Shear modulus	30	Gpa
20	$refvisc$	Reference viscosity	0.125e-17	Pa ⁻ⁿ /s
21	$activationE$	Activation Energy	276.0e+3	kJ/mol
22	vis_{min}	viscosity minimum cutoff	1.0e+18	Pa * s
23	vis_{max}	viscosity maximum cutoff	1.0e+27	Pa * s
24	$srexponent$	Power of power law in viscosity	3.05	N/A
25	$\varepsilon_{p_i}^1$	initial plastic strain for piecewise Type 1 weakening	0	N/A
26	$\varepsilon_{p_i}^2$	initial plastic strain for piecewise Type 2 weakening	0	N/A
27	$\varepsilon_{p_e}^1$	end plastic strain for piecewise Type 1 weakening	0.1	N/A
28	$\varepsilon_{p_e}^2$	end plastic strain for piecewise Type 2 weakening	0.33	N/A
29	C_i	initial Cohesion for piecewise weakening	44	Mpa
30	C_e	end Cohesion for piecewise weakening	4	Mpa
31	ϕ	Friction angle	30	°
32	$remesh_{timestep}$	Remesh when timestep reach its value	400000	N/A
33	$remesh_{length}$	Remesh when the global minimum of the ratio of the volume of a tetrahedron to one of its surface area	0.6	N/A
34	$topTemp$	Surface temperature	0	°C
35	$bottomTemp$	Bottom temperature	1300	°C
36	V_x	Half spreading rate	7.9e-10	m/s

Table 2: List of 3D numerical experiments.

Model	M range	Functional Form	Type of weakening	For short
1	M28	Linear	Type 1	M28LinT1
2	M28	Sinusoidal	Type 1	M28SinT1
3	M28	Square Root	Type 1	M28SqrtT1
4	M57	Linear	Type 1	M57LinT1
5	M57	Sinusoidal	Type 1	M57SinT1
6	M57	Sinusoidal	Type 2	M57SinT2
7	M57	Square Root	Type 2	M57SqrtT2
8	M58	Sinusoidal	Type 1	M58SinT1
9	M58	Sinusoidal	Type 2	M58SinT2
10	M58	Square Root	Type 1	M58SqrtT1
11	M58	Square Root	Type 2	M58SqrtT2
12	M88	Constant	Type 2	M88ConT2

3 Results

In this “Results” chapter, I first walk through the reference model (M28LinT1) and compare it with a constant M model (M88ConT2). Then, I describe in detail the seven major characteristics of the models. Finally, I describe the effects of different weakening rates, ranges as well as functional forms of M variation on the main characteristics.

3.1 Reference model M28LinT1

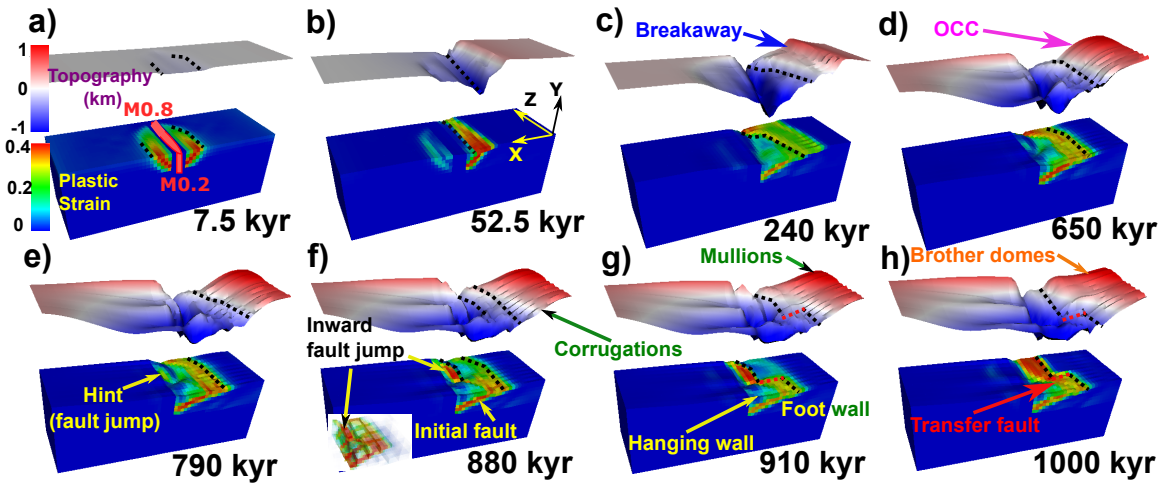


Figure 8: Evolution of plastic strain and surface topography of the reference model M28LinT1 (Table 2). Each snapshot shows plastic strain plotted on the model domain and the five times exaggerated topography. Initial seafloor is marked as a reference of 0 km of the topography. The black dashed lines are the terminations of the detachment faults. The red dashed lines in g) and h) are the transfer faults that connect the terminations along the ridge. The inset in f) plots plastic strain with opacity linearly proportional to its value.

I consider the model with M varies linearly from 0.2 to 0.8 along the ridge axis with type 1 weakening rate (M28LinT1) as the reference model. The major structural features of the model are indicated in the Figure 8. They are breakaway (Figure 8.c); oceanic core complex (OCC) (Figure 8.d); termination of the detachment fault along the ridge where the active faulting interface reaches the seafloor (black dashed lines); new high angle normal faults forming near the ridge axis (Figure 8.f), which is termed as “inward fault jump” (Tucholke et al., 1998); corrugations (Figure 8.f) and mullion structures (Fig-

ure 8.g); and the side-by-side “brother domes” (Figure 8.h).

The model produces a median valley that widens and deepens with increasing plate extension (Fig. 8a-c). The rate of its widening and deepening at a specific location along the ridge is inversely proportional to the M value (i.e. rate of local magma supply).

For the first 7.5 kyr (Figure 8.a), normal faults, represented by localized plastic strain, begin to form near the ridge axis. Because stresses due to plate extension accumulate faster at the lower M side than at the higher M side, faults first initiate at the lower M side and then propagate to the higher M side. The asynchronous initiation of faults along the ridge axis creates offset in breakaway: i.e., the breakaway at the lower M side moves further away from the ridge axis than that of the higher M side (Figure 9).

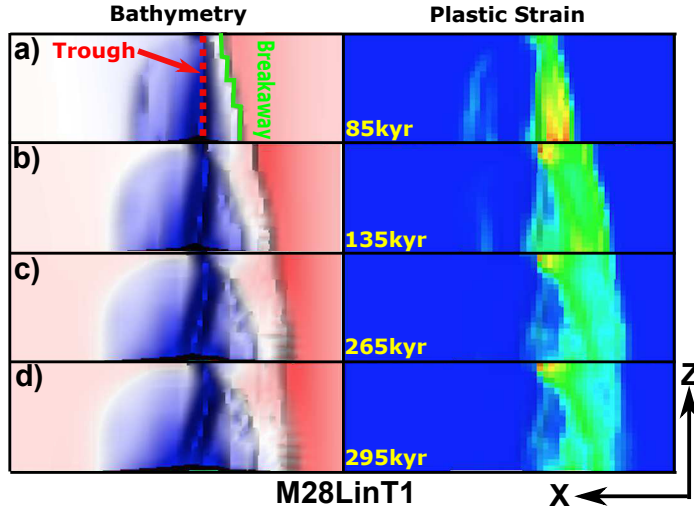


Figure 9: Bird's-eye view of the evolution of breakaway (marked by green bold line) and depressed narrow zone (“trough”) along the ridge axis (red dashed line in (a)). This figure share the same color scales with Figure 8.

By 52.5 kyr (Figure 8.b), the normal fault on the right hand side of the ridge axis remains active while the one on the left becomes inactive. As the fault on the right hand side evolves, the upper part of the fault plane (shown as plastic strain in the model) is exhumed to the seafloor. Initially, the edge of this permanently deformed fault interface that is moving away from the ridge axis corresponds to the right boundary of the plastic strain. By 265 kyr (Figure 9.a~c), the right boundary (tips) of the plastic strain also aligns

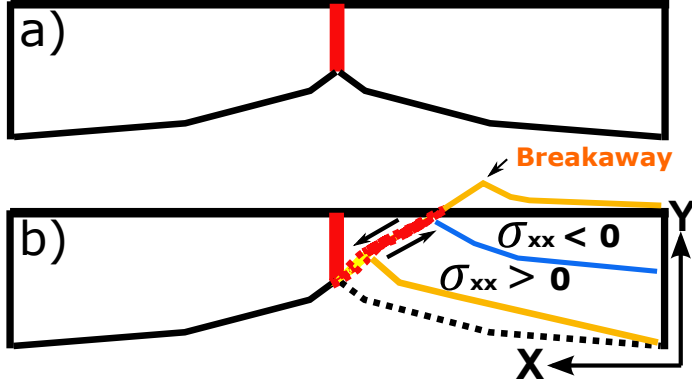


Figure 10: Bending stress illustration. The blue line is the neutral plane where $\sigma_{xx} = 0$. Above the neutral plane is compression ($\sigma_{xx} < 0$) and beneath it is tension ($\sigma_{xx} > 0$).

with the breakaway along the ridge. The along-ridge offset in x -direction of the tips of the moving plastic strain reduces at ~ 295 kyr (Figure 9.d) because when the normal fault lasts long enough and rotates to its minimum dip angle at the lower M side at ~ 240 kyr (Figure 9.c), the termination of the detachment fault stops moving further away from the ridge axis and the healing effects (following Tucholke et al., 2008) implemented in the model reduces quickly the plastic strain of the historical fault interface that has been exhumed to the seafloor. While at the higher M side, the termination keeps moving away from the ridge axis and gradually catches up with the termination at the lower M side in negative x direction. This reduces the initial offset generated by the asynchronous initiation of faulting. In addition, as the fault slips, crust at the footwall bends in a clockwise rotation as illustrated by Figure 10.

The active, near-axis normal fault rotates to a lower dip of $\sim 30^\circ$ at the root of the fault and to $\sim 0^\circ$ at the exposed fault interface (Fig. 8.c). However, the normal fault at the higher M side (especially for $M > 0.7$) experiences less fault rotation and the termination of the fault is closer to the ridge axis. The maximum relief between the breakaway and the trough inside the median valley becomes larger than 1 km. In addition, ~ 2 km wavelength corrugations begin to show up between the breakaway and termination at the lower M side ($M < 0.3$). The corrugations show a uniform wavelength which is smaller than that of the mullion structures (Figure 8.g). Formation mechanism for these structures are

discussed in one of the following sections. The trough is initially straight and parallel to the ridge axis (Figure 9.a) but becomes oblique to the ridge axis. The obliquity increases with the amount of extension (Figure 9.b~d).

By 650 kyr (Figure 8.d), the median valley becomes wider and deeper. The detachment fault reaches its lowest dip angle and its termination stops moving away from the ridge axis. The breakaway of this detachment has already moved out of the model domain. The total fault offset at this point is greater than the thickness of the crust and thus sufficient for exhuming the upper mantle materials.

By 790 kyr, a hint of the new near-axis fault first appears at the center fo the model domain with $M \in (0.5, 0.65)$ and then propagates in a positive z direction (Fig. 8.d,e). At this time, the initial detachment fault is still active and takes up most of the extension.

By 880 kyr, the new near-axis normal fault at the higher M side cuts through the hanging wall of the detachment fault (Fig. 8.f). It coexists with the initial detachment fault and begins to accommodate most of the intra-plate extension. This event is called the “inward fault jump” [Tucholke et al., 1998; Dick et al., 2008].

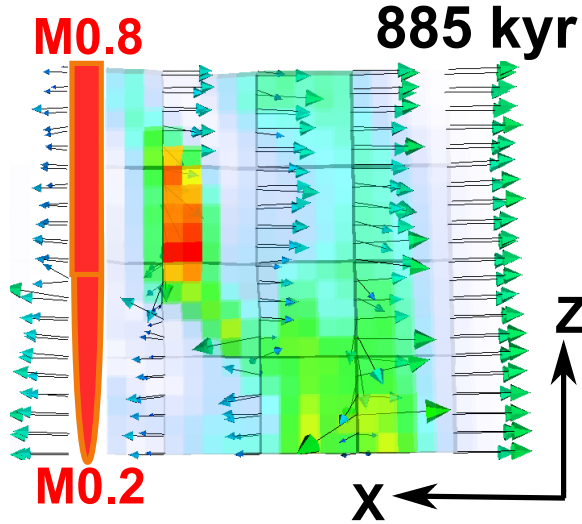


Figure 11: Bird's-eye view of velocity field with plastic strain plotted with ^{EC:} opacity [why do you need transparency in this figure?] ^{XT:} if not transparent, the velocity vectors will be hidden linearly proportional to its value. (color scale is the same as Figure 8.a))

By 910 kyr (Fig. 8.g), the inward fault jump completes in the $M > 0.5$ region: the new

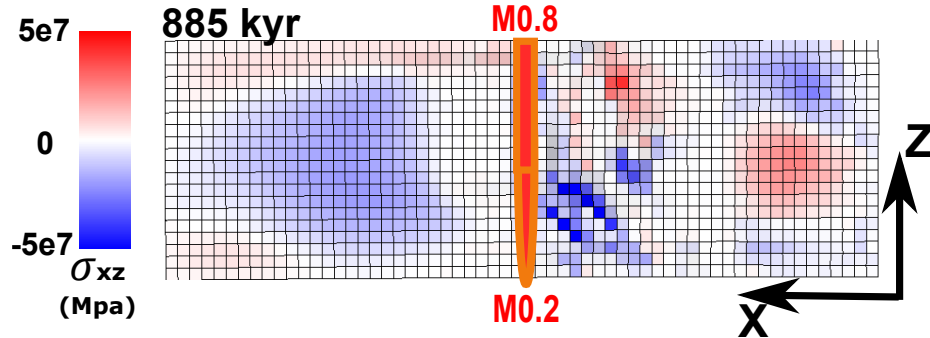


Figure 12: Bird's eye view of σ_{xz} .

high-angle fault takes up all the extension and the initial detachment fault becomes completely inactive. The block that was previously a hanging wall to the detachment becomes footwall of the new fault and moves with the spreading plate to the negative x -axis direction. At the lower M side, the detachments is still active and the hanging wall continues to move toward the positive x -axis direction (Figure 11). This opposite sense of relative motions between the high and the low M side produces a region of dextral shear and eventually creates a transfer fault (Fig. 8.h).

As the inward jumped fault evolves, another dome adjacent to the initial OCC is produced at the higher M side by 1000 kyr (Fig. 8.h).

3.1.1 Constant M model M88ConT2

^{XT:} I still prefer to have M88ConT2 because: 1. As a comparison to the varying M model, it help to show the importance of M variation (corrugation, mullion, median valley variation, inward fault jump etc. 2. it itself is a mode of MORs topography formation mechanism, those higher frequency symmetrical abyssal hills.

As a comparison to the varying M models, a constant M model is run.

As shown in Figure 13, model M88ConT2 pruduces a ~20 km wide and 1~2 km deep median valley, which is similar to the generally observation of the Mid-Atlantic Ridges. The width and depth of the median valley is almost constant along the ridge as contrast to the varying M models. The variation of the location of the breakaway and ter-

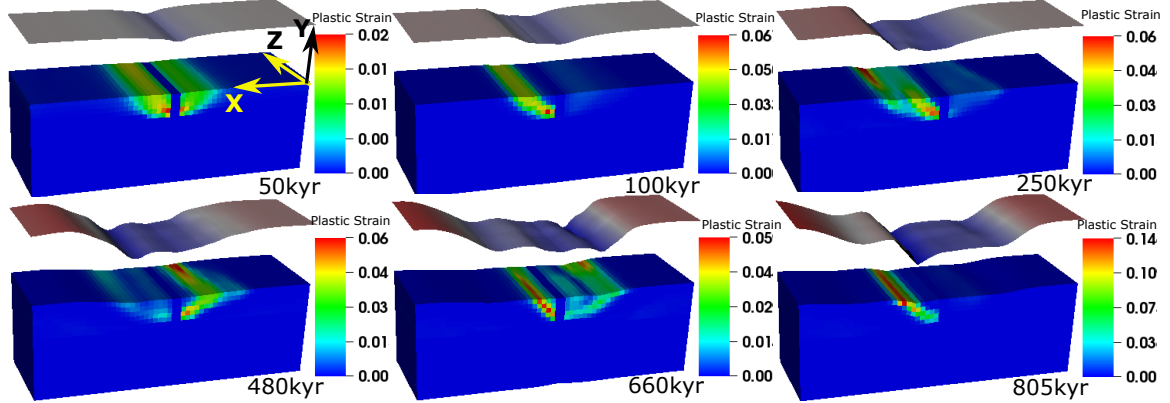


Figure 13: Evolution of plastic strain and surface topography of the model: M88ConT2 (Table 2). (color scale of topography is the same as Figure 8.a)

mimation along the ridge that is mentioned in the reference model (M28LinT1) does not show up. Because the magma supply is constant along the ridge with $M = 0.8$, there is no stress perturbation along the ridge. Thus, the normal faults along the ridge initiate at the same time and the slipping rate of the fault is also constant along the ridge axis. The synchronized fault initiation results in no offset between breakaways and the constant slipping rate produces no along ridge axis variation in the position of the termination. In addition, neither corrugations nor mullion structures are generated. Normal faults alternate on each side of the ridge axis with a period of ~ 300 kyr due to the mechanism metioned in the “Introduction” section for the 2D models of $M > 0.5$. This fault alternaltion produces symmetrical high frequency abyssal hills. For 3D models, why and how fault alternates on each side of the ridge axis is different from the previous 2D studies and is described in the following sections.

3.2 Main characteristics of the models

I identify seven features that are common to most of the models: location of the termina-
tion, geometry of the trough, inward fault jump, fault alternation, mass wasting, hourglass-
shaped median valley and corrugations and mullion structures. Since the details of these
features differ among the models, they are useful for delineating and contrasting compli-

cated model behaviors.

3.2.1 Location of termination

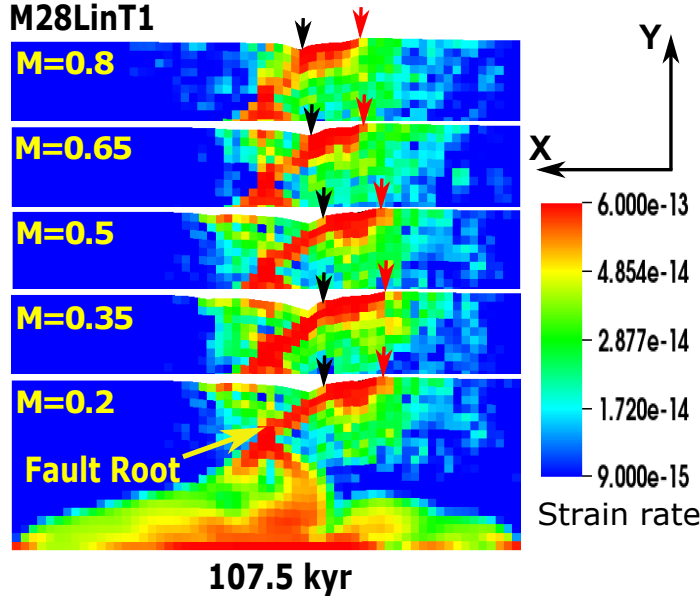


Figure 14: The second invariant of strain rates plotted on the reference model’s vertical cross-sections along the ridge at 107.5 kyr. Terminations and breakaways are marked by black and red arrows.

The location of the termination is delineated by black dashed lines in Figure 8 and marked by black arrows in Figure 14. It varies along the ridge due to the variation in M value.

When $M \leq 0.5$, the distances between the termination and the ridge axis as well as the dip angles of the detachment fault are similar. Because the rotation rate of the detachment fault is determined by how fast the termination move away from the fault root. Since the detachment faults for the ridge region of $M < 0.5$ root at the same place at the intersection between the center dike and the brittle-ductile transition (BDT) and the moving rate of the termination has a maximum value that is restricted by the far field extension rate V_x , the distances between the terminations and fault roots of the detachment faults is similar among the three slices of $M \leq 0.5$. In addition, in order to spend least frictional energy during faulting, the detachment fault interface between the two ends (termination

and fault root) tends to be a straight line. Thus, the dip angle of the detachment fault is inversely proportional to the distance between the termination and the root of the fault when $M < 0.5$. Since the termination at the lower M side ($M < 0.5$) moves with the spreading plate with same velocity V_x , and the initiation time difference of the normal faults at the lower M side is similar (Figure 8.a), the distances between the terminations and the roots of the faults are the same. Thus the dip angles as well as the distance between the termination and the ridge axis of the faults at the lower M side are similar. However, when $M > 0.5$ (Figure 14, ($M = 0.65, 0.8$)), the amount of fault slip decreases as M increases. The crust at the footwall experiences less bending and the detachment fault remains in a higher angle as well as that the terminations are closer to the ridge axis. Because the root of the fault is slowly pushed away from ridge axis while the termination of the faults are closer to ridge axis due to a later initiation of the fault. One thing needs to be noted is that the trough at the higher M side correspond to the terminations but detached from the terminations at the low M side ($M < 0.5$) as shown in Figure 14.

3.2.2 Geometry of trough

The depressed narrow region inside the median valley is termed as “trough”. The reference model showed that its shape in the map view evolves from a straight line parallel to the ridge axis to a line oblique to the ridge axis (Figure 9). Initially, the trough along the ridge corresponds to the termination. However, at the lower M side ($M < 0.5$), as the normal fault rotates to a lower dip at the lower M side, the trough is no longer coincident with the fault termination and is moving slowly to the left because the hanging wall is pulled by the conjugate plate. However, the trough on the higher M side ($M > 0.5$) is pushed away from the ridge axis [Tucholke et al., 2008]. But since the trough cannot bypass the termination, the trough at $M = 0.8$ is restricted closer to the ridge axis. Together it generates the curved shape of the trough (Figure 9).

3.2.3 Inward fault jump

The inward fault jump occurs in all the models when an old fault locks and a new one forms near the ridge axis (e.g., Fig. 8). ^{XT:}[for the description of the previous commented out paragraph, please refer to:\[Lavier et al., 2000; Olive et al., 2014\]](#)

The new fault usually forms on the high M side first and it connects to the existing detachment developing on the lower M side ($M < 0.5$), producing a curved fault termination. Unlike fault alternation, the inward fault jump occurs on the same side of the ridge axis with its along-axis extent corresponds to the $M > 0.5$ region.

3.2.4 Fault alternation

When M is high enough, a normal fault first forms on one side of the ridge axis but another fault forms on the other side when the first one locks (Fig. 13) [Buck et al., 2005, Tucholke et al., 2008]. This behavior is termed as “fault alternation”.

3.2.5 Mass wasting

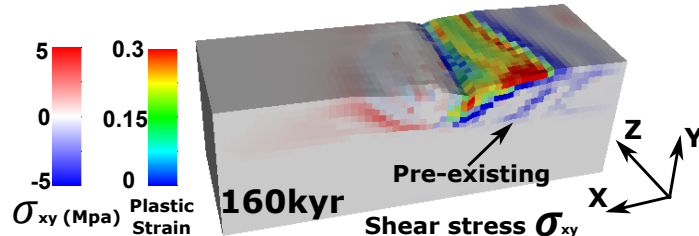


Figure 15: The weak detachment fault tip reaches the pre-existing shear stress. Plastic strain is plotted with opacity linearly proportional to its value.

Mass wasting occurs on the exposed surface of a low-angle normal fault. When a layer of weak fault interface becomes gravitationally unstable and is detached from the underlying material, the detached layer flows towards the ridge axis and the lower M side with a velocity ~ 10 times faster than the half spreading rate (Figure 16; Figure 17.b,e (first row))). The mass wasting produces a continuous fault scarp with a relief of ~ 1 km along the initial breakaway.

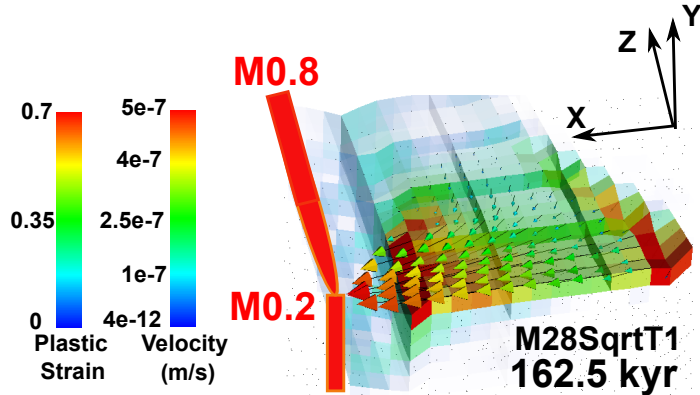


Figure 16: Velocity of the mass wasting hanging wall. Magnitudes of the velocity are shown by the colors of the arrow heads. Plastic strain is plotted with opacity linearly proportional to its value.

Immediately after an event of mass wasting, the fault trace jumps towards the ridge axis (Figure 17.d versus f (third row: plastic strain)). Then, σ_{xy} and σ_{xz} soon ^{EC:} fill in the area [What do you mean by “stresses filling an area”?] between cut-back created fault scarp and the new termination (Figure 17.f (fourth and fifth row: σ_{xy} and σ_{xz})). ^{EC:} [don’t understand the rest of this paragraph.] After that, the termination at the higher M side extends faster and further than the lower M side (Figure 20.a~d). This is because during the cut-back, tensional stress due to bending is released at the lower M side but continues to accumulate at the higher M side. At the lower M side, it needs time to reach the previous tensional stress state and then starts from there to pull the new termination away from the ridge axis. While at the higher M side the increasing tensional stress directly leads to a fast extending termination.

3.2.6 Hourglass-shaped median valley

A median valley takes a hourglass shape whenever M varies along the ridge. The hourglass shapes vary with time and the functional form of M variation. A median valley initially has similar width along the ridge but is deeper on the lower M side where normal faults first form. By ~ 100 kyr (Figure 21.b), the fault on the negative x -axis direction of the ridge axis doesn’t propagate to the higher M side of the ridge and becomes inactive.

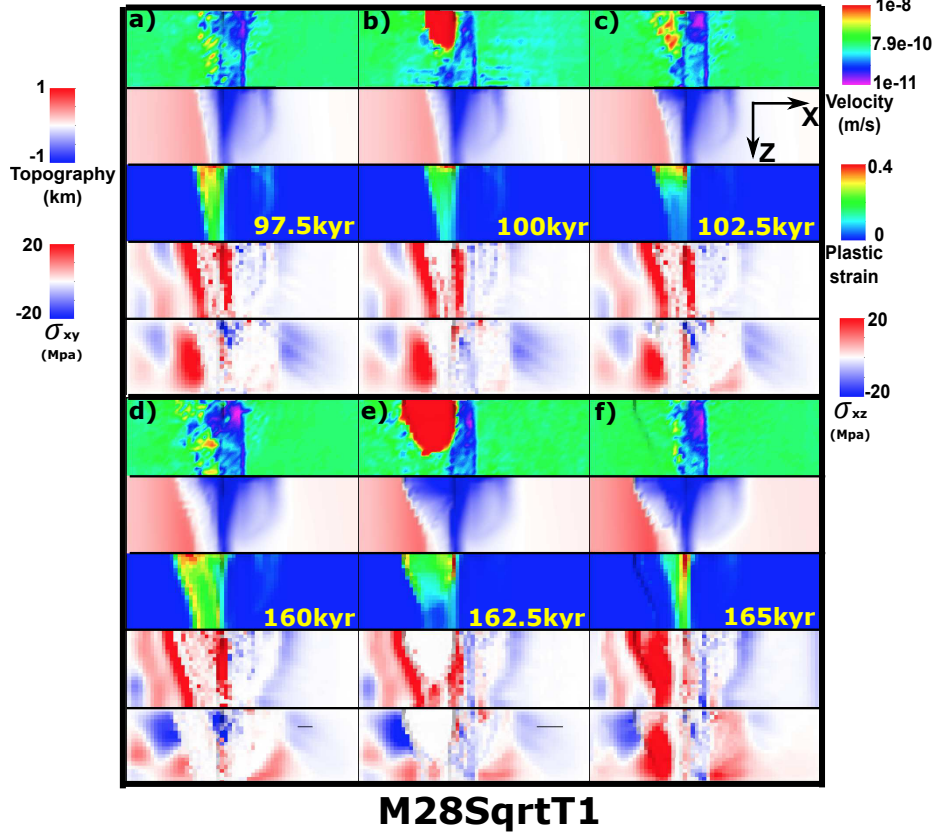


Figure 17: Plastic strain, topography and stresses evolution for M28SqrtT1.

It produces a depressed topography curve following the inactive fault trace, which is further away from the ridge axis at the lower M side but closer to ridge axis at the higher M side. On the other side of the ridge axis, as the active fault rotates to a lower dip angle, it generates breakaways that are further away from the ridge axis at the lower M side while closer to the ridge axis at the higher M side. This along ridge variation in the location of the breakaways act as another boundary of the hourglass. Both boundaries are extended following the spreading plates. By ~ 170 kyr (Figure 21.c), the hourglass become wider and deeper. Since the area of the cross-section along the ridge inside the hourglass shape median valley is approximately inversely proportional to the local M values, the shape of the hourglass varies with different M variations.

The further depression inside the median valley is mostly due to the elastic deformation from crustal extension. As shown in Figure 22, the σ_{xx} in the median valley is higher

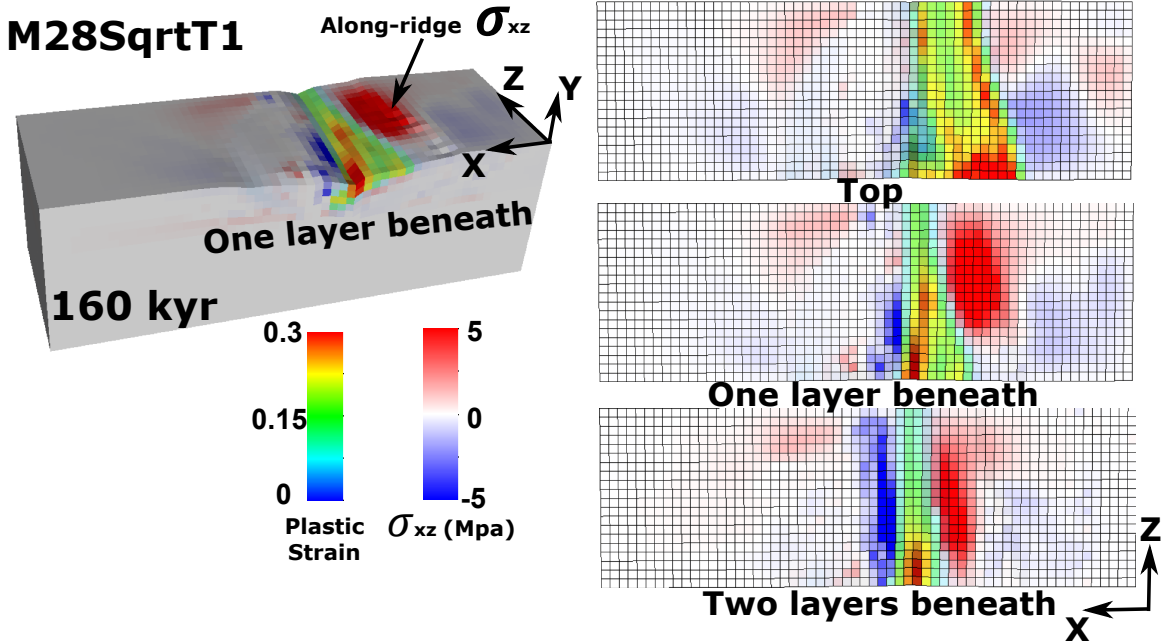


Figure 18: Along ridge axis σ_{xz} (bird's-eye view of three layers of model domain) (positive(red) means clockwise). Plastic strain is plotted with opacity linearly proportional to its value.

because that the brittle crust is the thinnest at the median valley, when same amount of force propagates from far field extension to the median valley, the stress increases. This increased σ_{xz} is responsible for the further depression and extension of the median valley on the negative x -axis direction of the ridge axis (Figure 21.d). For the median valley on the other side of the ridge axis, cut-back triggered mass wasting between the breakaways and the ridge axis results in the further lowering in topography (Figure 17.d versus e (topography)).

3.2.7 Corrugations and mullion structures

Both corrugations and mullion structures are linear structures parallel to the spreading direction. As shown in Figure 8.f, at the $M < 0.5$ area on top of the OCC surface, corrugations show a uniform wavelength of ~ 2 km with hundreds meters in amplitude. While at the higher M side of the ridge (Figure 8.g), a mullion structure of a wavelength of ~ 7 km. In spite of morphological similarity, corrugations and mullion structures have differ-

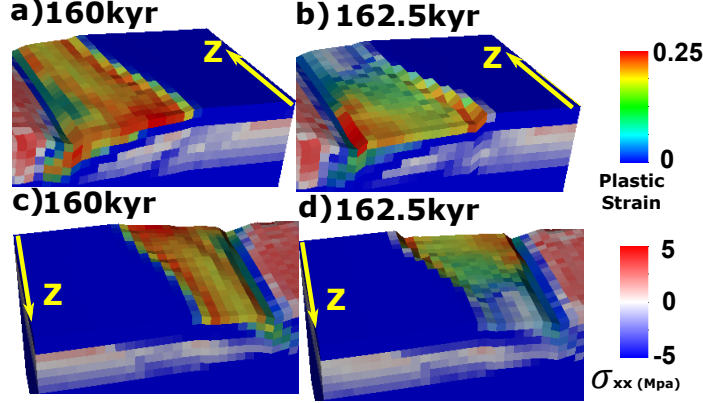


Figure 19: M28SqrtT1 (Table 2). Bending stress drop (a versus b) at the lower M side due to the cut-back. No bending stress drop (c versus d) at the higher M side as a comparison.

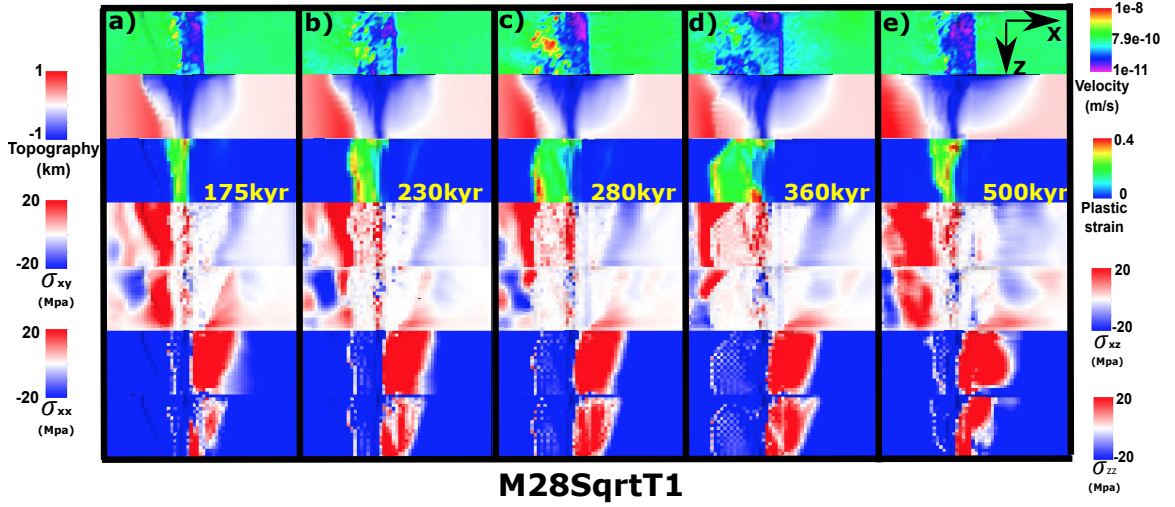


Figure 20: New fault front chase after cut-back.

ent formation mechanisms.

Corrugations

The corrugation starts at the breakaway as a response to tensile stress in the z -axis direction. As shown in Figure 23, when the plastic strain reaches or exceeds 0.1 (red color), based on type 1 weakening, the cohesion decreases to 4 Mpa. With a 30° friction angle, tensile failure is declared when the σ_{zz} reaches ~ 7 Mpa (yellow color). The tensile stress is due to the asynchronous faulting along the ridge. Faulting initiates earlier at the lower M side of the ridge. As the fault offsets more on the low M side than on the high M side,

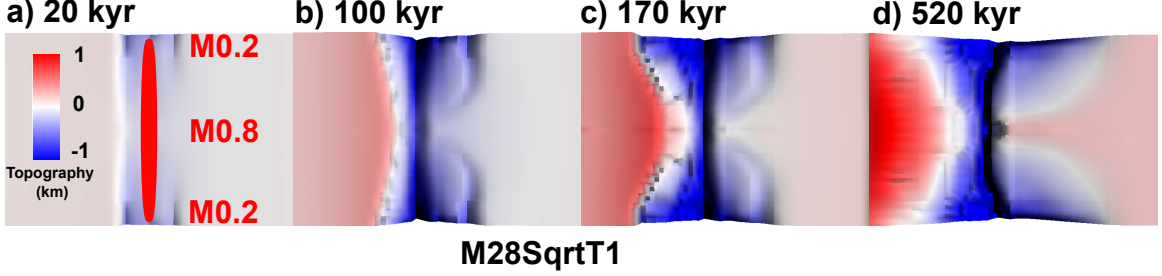


Figure 21: Bird's-eye view of the evolution of the hourglass shape median valley. It is generated by attaching the topography of the M28SqrtT1 model to its mirror reflection by assumming symmetrical M variation (0.2 to 0.8 to 0.2).

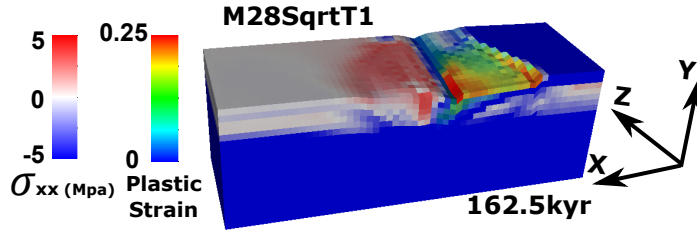


Figure 22: Higher σ_{xx} shows inside the median valley on the negative x -axis direction of the ridge axis.

the footwall of the fault rotates and get uplifted more on the low M side. The footwalls along the ridge generates the isochron-parallel tesimal stress σ_{zz} . Since σ_{zz} follows along the moving tip of the plastic strain, the plastic strain together with σ_{zz} generate tensile failure that extends away from the ridge axis and thus produces the linear corrugations that are parallel to the spreading velocity. Detail analysis along with simpler model experiments are given in the “Discussion” section.

Mullion structures

Mullion structures observed in the models are formed by the along ridge variation in the location of the termination due to the evolution of faulting. They usually appear at where the termination is closer to the ridge axis. The shape of the footwall follows the trace of the termination as it is exhumed to the surface. At where the termination is bent inward to the ridge axis, an “initial dome” (Figure 24.a) is produced once the hanging wall is exhumed to the seafloor. The wavelength of the mullion structure is determined by

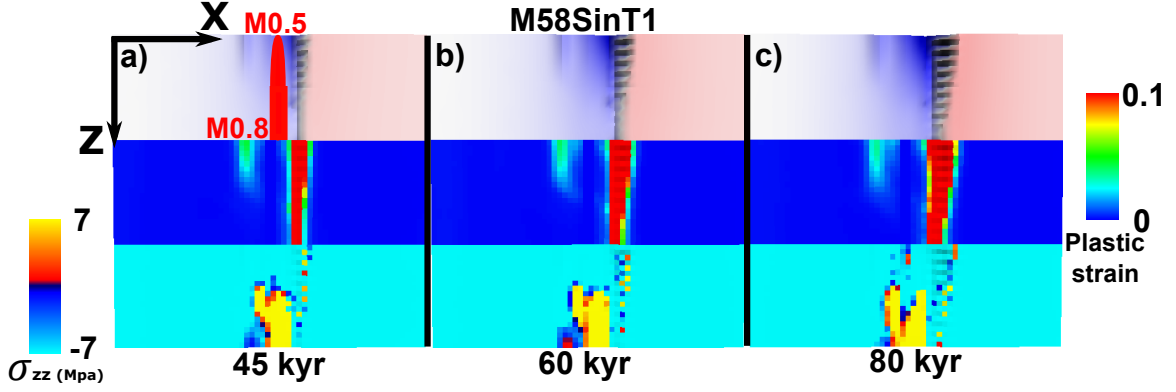


Figure 23: Bird's-eye view of the evolution of the corrugations. Color scales for the topography is the same as Figure 8.

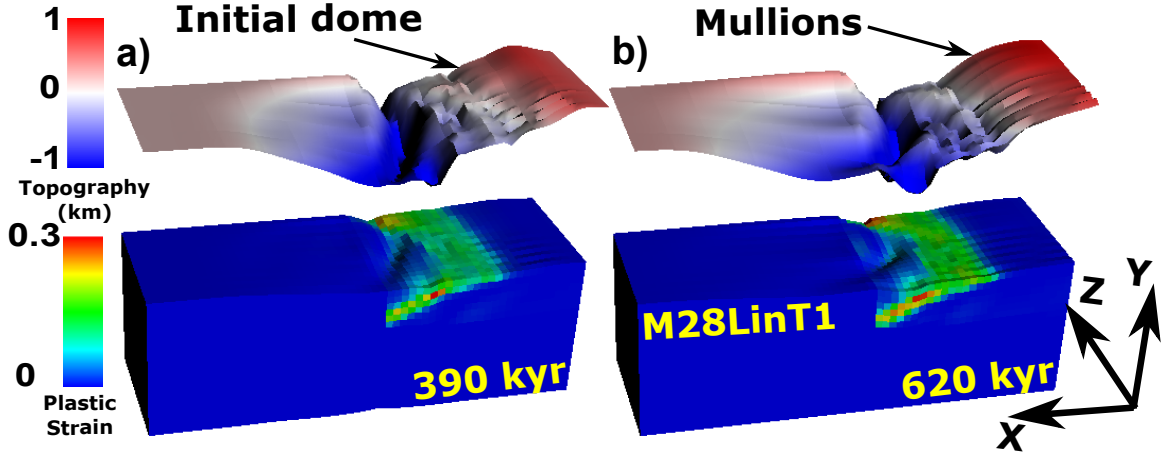


Figure 24: Evolution of mullion structures.

the shape of the termination. If the pattern of the termination lasts for a long time and the footwall of the detachment fault keeps being exhumed to the surface following the trace of the detachment fault termination, a mullion structure is produced (Figure 24.b)).

3.3 Effects of the functional forms of M variation

3.3.1 M28(Lin, Sin, Sqrt)T1

Comparing M28LinT1, M28SinT1 and M28SqrtT1, major differences lie in the model behaviors of the “inward fault jump”, the “cut-back” and the “hourglass shape median valley”. All three models have no fault alternation.

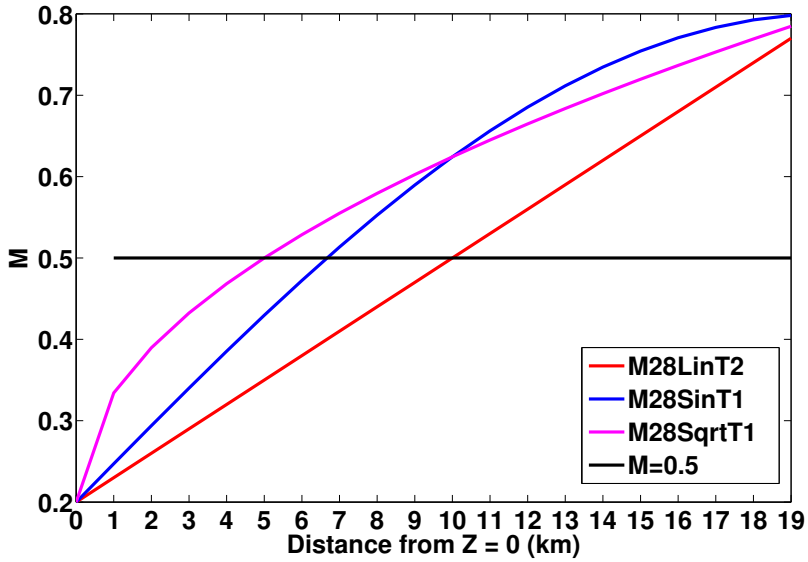


Figure 25: Three functional forms of M variation. M begins to exceed the $M = 0.5$ black line at $Z=10$ km, 7 km, 5 km for M28LinT1, M28SinT1 and M28SqrtT1 respectively.

Inward fault jump

Only linear and sinusoidal models have inward fault jump. Square root model shows no inward fault jump because during cut-back, termination of the detachment fault retreats backward toward the ridge axis and the detachment fault is maintained near the ridge axis.

Between linear and sinusoidal models, timing and dimension of the inward jumping faults are different. For the linear functional form, the inward fault jump at the higher M side starts accommodating most of the extension at ~ 900 kyr and replaces the initial detachment fault (Figure 26, Figure 8.f). It nucleates from the ridge center where $M = 0.5$ and then propagates to the $M = 0.8$ end with a length of ~ 11 km. For the sinusoidal functional form, the inward fault jump takes the place of the initial detachment fault earlier at ~ 550 kyr with a length of ~ 14 km (Figure 26).

The timing difference between the linear and sinusoidal models is because M28SinT1 consistently has a higher M values than the M28LinT1 (Figure 25), which results in that the initial detachment fault at the higher M side ($M > 0.5$) of M28SinT1 is pushed off

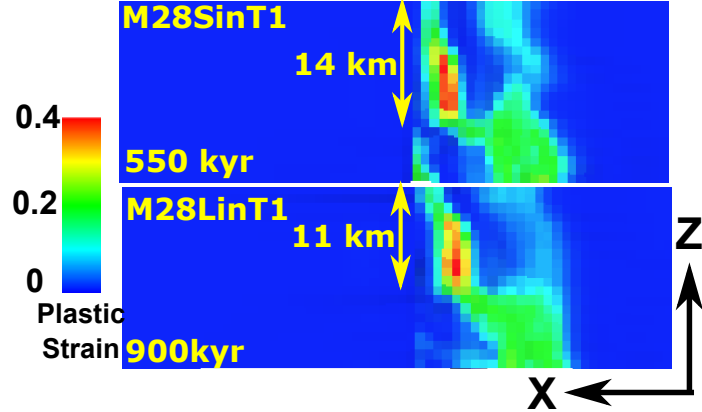


Figure 26: Bird’s-eye view for comparing the length and timing of inward fault jump.

axis faster than M28LinT1 and thus forming an earlier inward fault jump. The length difference is because M28SinT1 has a greater length along the ridge axis of $M \geq 0.5$ (Figure 25).

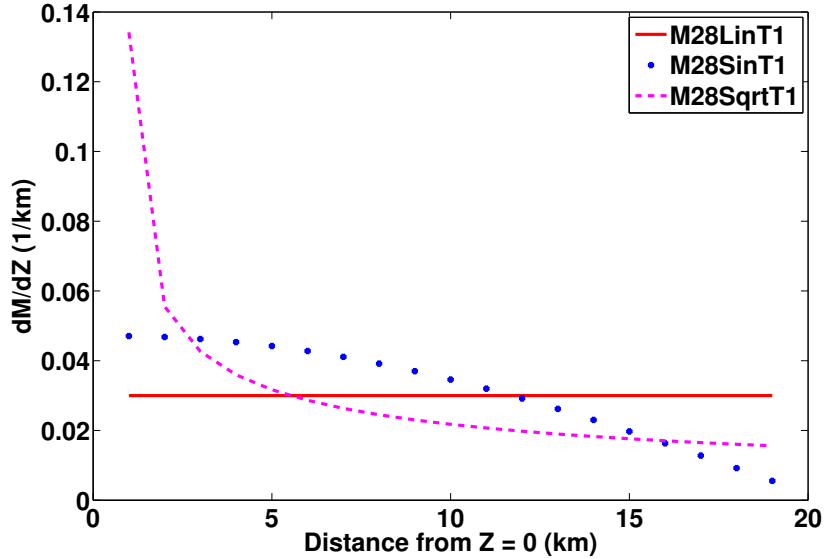


Figure 27: $\partial M / \partial Z$ comparision.

Cut-back

Cut-back only happens in the M28SqrtT1 model. Qualitatively, it is because M28Sqrt has a much higher value of $\frac{\partial M}{\partial Z}$ at the lower M side (Figure 27), which implies a larger along ridge shear stress σ_{xz} as well as a larger difference in σ_{xy} along the ridge that result

in the decoupling between the higher and lower M sides hanging walls.

Hourglass shape median valley

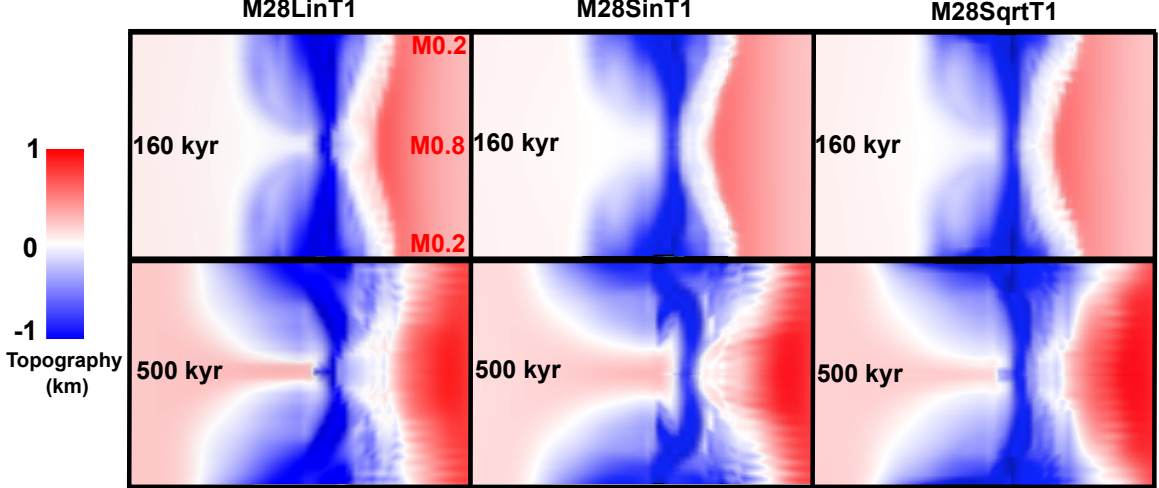


Figure 28: Bird's-eye view of the topography. (without vertical exaggeration.)

As shown in Figure 28, differences among the three models are identified. At 160 kyr, median valley for M28SinT1 has the smallest cross-section ($x-y$) area at the higher M side. While at the lower M side, M28SqrtT1 has the smallest area of the cross-section. This is because the cross-section area inside the median valley is inversely proportional to the local M value along the ridge. Moreover, the breakaways at the lower M sides for M28LinT1 and M28SinT1 bend to parallel to the ridge axis while the breakaway for M28SqrtT1 extends further away from the ridge axis. In addition, M28SinT1 has a trough inside the median valley with the highest curvature. At 500 kyr, M28SinT1 has the narrowest median valley at the higher M side and the high topography zone on the left hand side of the ridge axis is the widest. Integrating the topography at the left hand side of the ridge axis of the three models, M28Sqrt has the largest value of integration since it has the largest integration of M along the ridge axis. In addition, the termination of the detachment fault of M28SqrtT1 has the highest curvature at the lower M sides. All these observations correspond to the M variation (Figure 25).

3.3.2 M58(Lin,Sin,Sqrt)T2

Table 3: Average M values of the 20 km segment. (The value is calculated by integrating M along the ridge axis and divided by the length of the model domain in z -axis.)

M range Function \ \diagdown	M28	M57	M58
Linear	0.4850	0.5950	0.6425
Sinusoidal	0.5668	0.6223	0.6834
Square root	0.5837	0.6279	0.6918

Among M58LinT2, M58SinT2 and M58SqrtT2, the major difference lies in whether it has “fault alternation”. Except for the constant M model M88ContT2, among all the models, only the models with type 2 weakening and M ranges from 0.5 to 0.8 (M58) have fault alternation. However, M58LinT2 does not produce alternating fault during the 1.1 Myr model time. Instead, one detachment fault lasts until ~ 300 kyr when the inward fault jump happens at the higher M side ($0.65 < M < 0.8$) and replaces the initial detachment fault. This provides an upper limit of average M value of the whole segment that prevent fault alternation and allows a long-lived detachment fault to produce a OCC. As shown in Table 3, the upper limit for the average M value is 0.6425 for M58LinT2. Detail analysis of the fault alternation is given in “Discussion”.

3.4 Effects of the weakening rate

Among the twelve 3D models, three pairs of models have both type 1 and type 2 weakening while the range of M and functional form are maintained to be the same. They are M57SinT1/T2, M58SinT1/T2 and M58SqrtT1/T2.

3.4.1 M57SinT1 versus M57SinT2

Initially, both models develop normal faults on both sides of the ridge axis at the lower M side. In the model with the faster weakening rate (M57SinT1), faults propagate toward

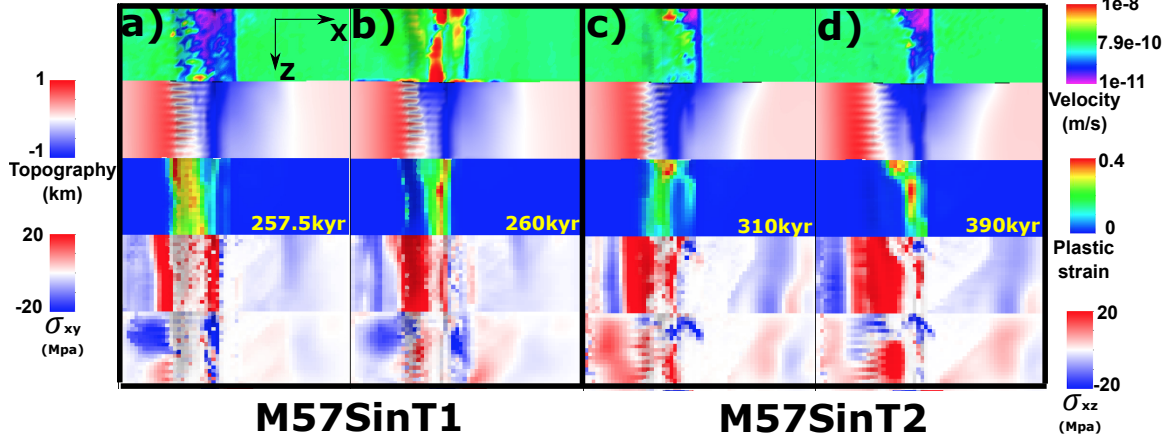


Figure 29: M57SinT2 versus M57SinT1 (Table 2)

the higher M side and cut through the whole crust by 25 kyr but this process completes later by 50 kyr in the model with the slower weakening rate (M57SinT2). By ~ 310 kyr, the inward fault jump appears at the higher M side ($M > 0.55$) of M57SinT2 while at where $M \leq 0.55$, the initial fault remains active (Figure 29.c and d). However, when the weakening is fast (M57SinT1), cut-back happens at ~ 260 kyr and helps to maintain a relative higher angle fault with a termination closer to the ridge axis. The initial fault remains, no inward fault jump forming (Figure 29.a and b). In addition, the width of median valley at the lower M side is wider for M57SinT2 than M57SinT1 (Figure 29.c, d versus a, b) because slower weakening (type 2) allows a more distributed tensile stress σ_{xx} rather than fast weakening that once a fault establishes, larger amount of the tensile stress σ_{xx} is released at the fault. The amplitude of the corrugations of M57SinT1 is larger than that of slower weakening M57SinT2. This is because faster weakening rate allows a faster decrease in the cohesion. As the cohesion reaches its minimum of 4 Mpa earlier when the plastic strain accumulates to 0.1, tensile failure is easy to happen in the isochron parallel direction and produces the corrugations.

M57SinT1

For M57SinT1, by 400 kyr (Figure 30.a), two antithetic fault forms at the lower M side ($0.5 < M < 0.58$) accommodating part of the plates extension. This makes the termi-

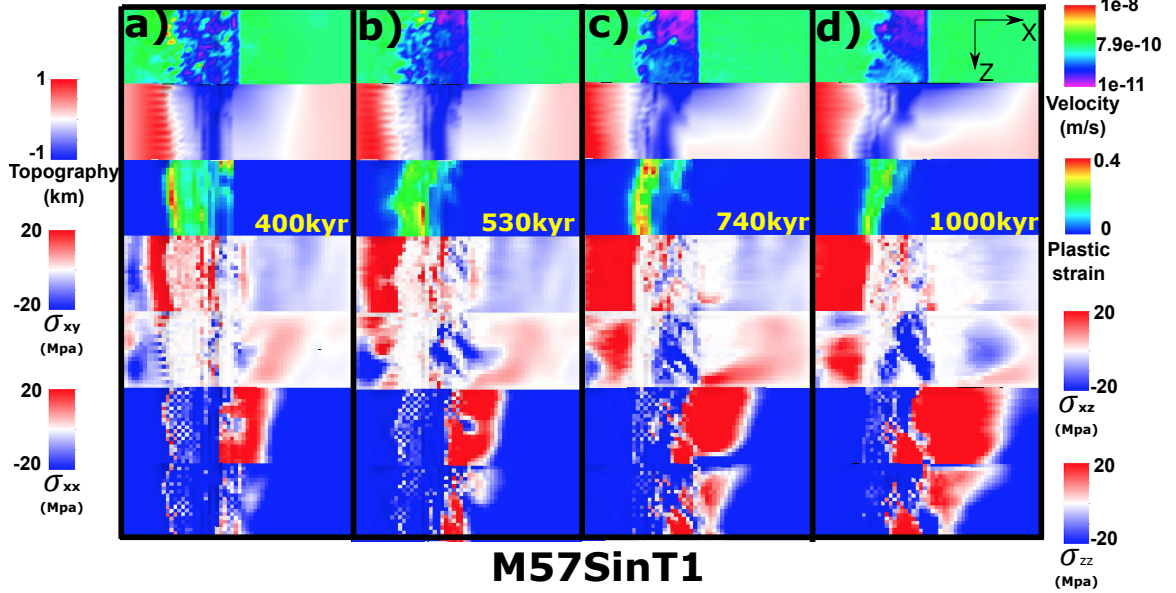


Figure 30: Faulting and stress evolution for M57SinT1.

nation at the lower M side retreat backward to the ridge axis. The hanging walls of the antithetic faults slide down into the trough and lower the topography. By 530 kyr, the termination at the center of the ridge segment ($M = 0.61\sim0.63$) extends further (Figure 30.b). This curved termination leads to a curved topography aligns with it (white curve in the second row). By 740 kyr, another antithetic fault forms at the lower M side (Figure 30.c). It doesn't take the place of initial fault and disappear soon, however, it again releases tensional stress and helps maintain a closer to ridge axis termination at the lower M side. By 1000 kyr (Figure 30.d), an Atlantiss Massif shape OCC is produced (lower M side has a wider dome and higher M side has a narrower dome) due to the along ridge termination evolution. Corrugations with wavelength varying from hundreds to kilometers are also produced.

M57SinT2

For M57SinT2, instead of maintaining a detachment fault like M57SinT1, it produces inward fault jump at the higher M side. By 325 kyr (Figure 31.a), an inward fault jump happens and takes the place of the initial detachment fault at the higher M side. Between

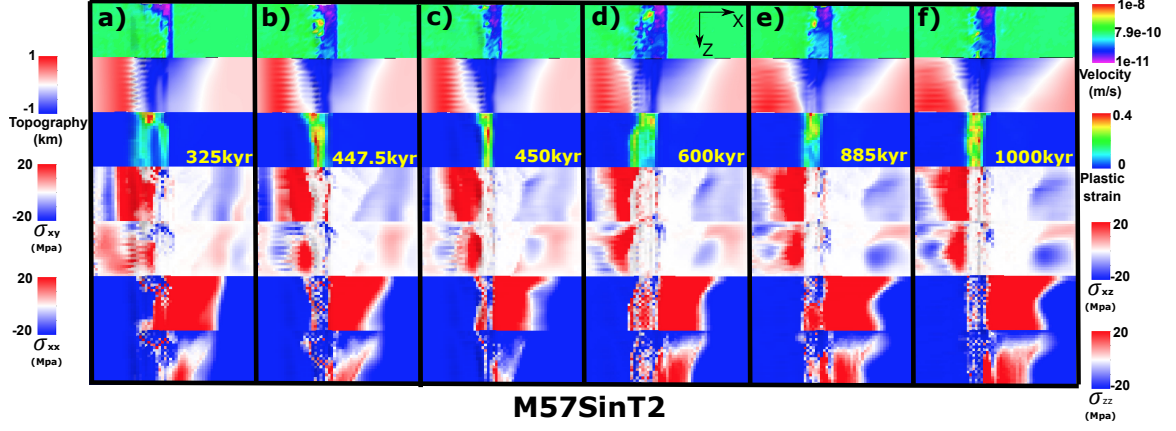


Figure 31: M57SinT2 (Table 2) faulting and stress evolution with respect to time.

447.5 kyr (Figure 31.b) and 450 kyr (Figure 31.c), a small scale cut-back happens and the termination recedes backward. By 600 kyr, the termination at the higher M side extends further (Figure 31.d). By 885 kyr, an inward fault jump happens at the higher M side ($0.62 < M < 0.7$) (Figure 31.e). The width of the median valley at the lower M side keeps increasing due to the distributed σ_{xx} (Figure 31.a~d).

3.4.2 M58SinT1 versus M58SinT2

A major difference between M58SinT1 and M58SinT2 is that only M58SinT2 has fault alternation.

M58SinT1

During the 1 Myr extension of the model M58SinT1, 10 phases of the evolution of faulting are identified (Figure 32.a~j). Antithetic faults, inward fault jumps, cut-backs happens and a rider block, corrugations and mullion structures are produced.

By 240 kyr (Figure 32.a), due to fast weakening (type 1), cohesion along the termination is low. Stress σ_{zz} takes the advantage and generates ~ 2 km wavelength corrugations parallel to the spreading direction as the termination extends further away from the ridge axis. Between 240 kyr (Figure 32.a) and 245 kyr (Figure 32.b), a cut-back happens with mass wasting at the lower M side. The termination recedes toward the ridge axis during

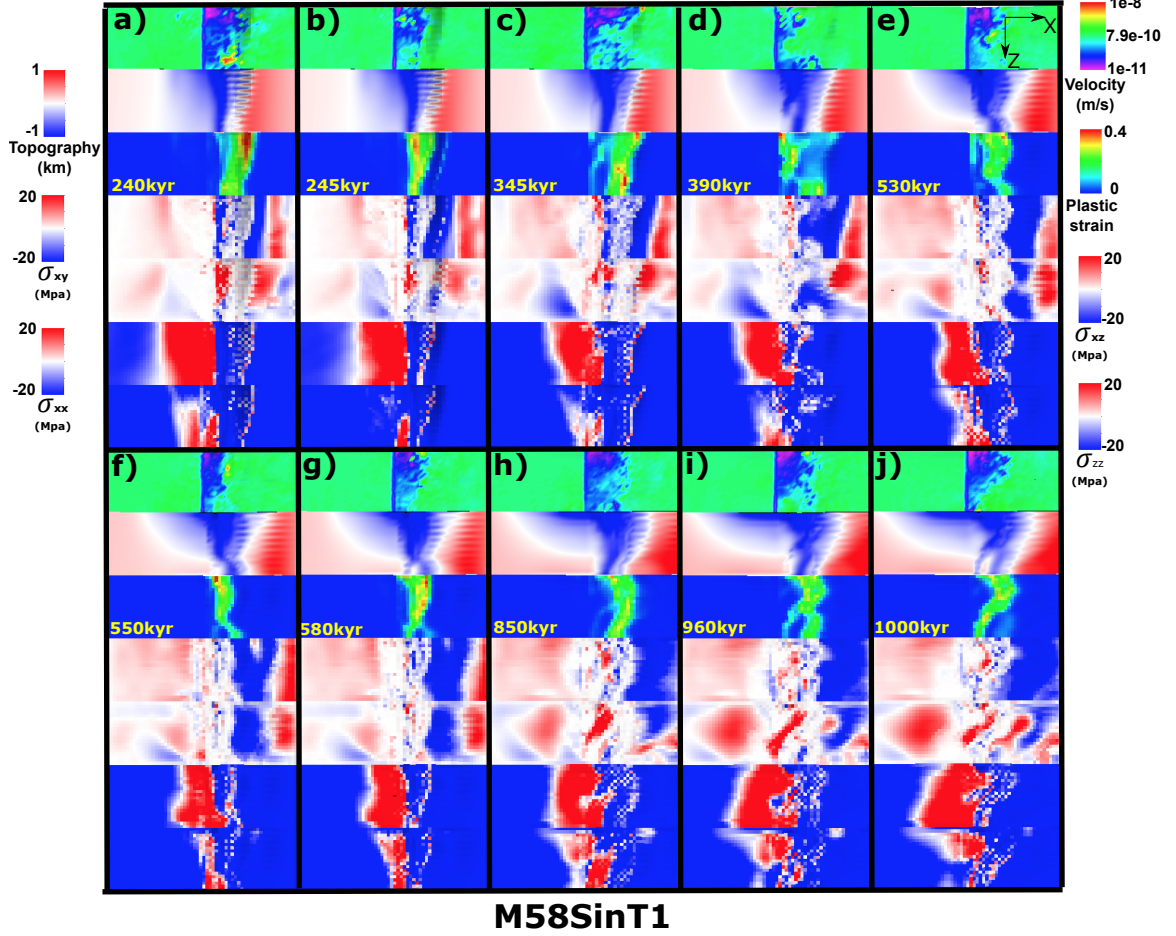


Figure 32: Faulting and stresses evolution (M58SinT1).

the cut-back. By 345 kyr (Figure 32.c), an antithetic fault forms at the lower M side ($0.5 < M < 0.545$) with an inward fault jump happens at ridge segment with $M \in (0.575, 0.635)$ (Figure 33). 45 kyr later, the two weak zone connect to each other and take the place of the initial detachment fault at the lower M side (Figure 32.d). Due to this inward fault jump, a dextral σ_{xz} zone (blue area in the σ_{xz} panel) forms and is bounded by the termination of the inward fault jump near the ridge axis at the lower M side and the termination of the initial detachment fault at the higher M side. By 530 kyr (Figure 32.e), the termination of the inward fault jump at the lower M side evolves to a curve with its center extends further away from the ridge axis because the inward fault jump initiates at the center and starts extending away from the ridge axis earlier, however, the lower M side of the curve remains closer to the ridge axis due to the antithetic fault and the other end of

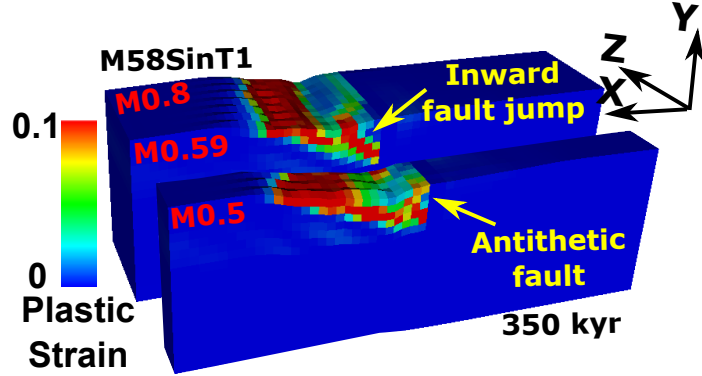


Figure 33: Plastic strain for M58SinT1 at 350 kyr.

the curve is also closer to the ridge axis because the fault initiates later. This curved termination at the lower M side also connects to the initial detachment fault at the higher M side which is further away from the ridge axis. Together, the curved termination is like a mirror reflected letter “S”. This flipped “S” shape termination is also reflected in topography. As the curved termination at the higher M side lasts for ~ 300 kyr since ~ 390 kyr, following the shape, a ~ 10 km in wavelength and ~ 7 km in along spreading direction mullion structure is formed (Figure 34). By ~ 680 kyr, an inward fault jump happens at the higher M side ($0.74 < M < 0.8$). It perturbs the curved shape termination and ceases the further exhumation of the mullion structure. This inward fault jump also produces a rider block that covers the inactive detachment fault and moves off axis following the exhuming footwall of the inward jumped fault.

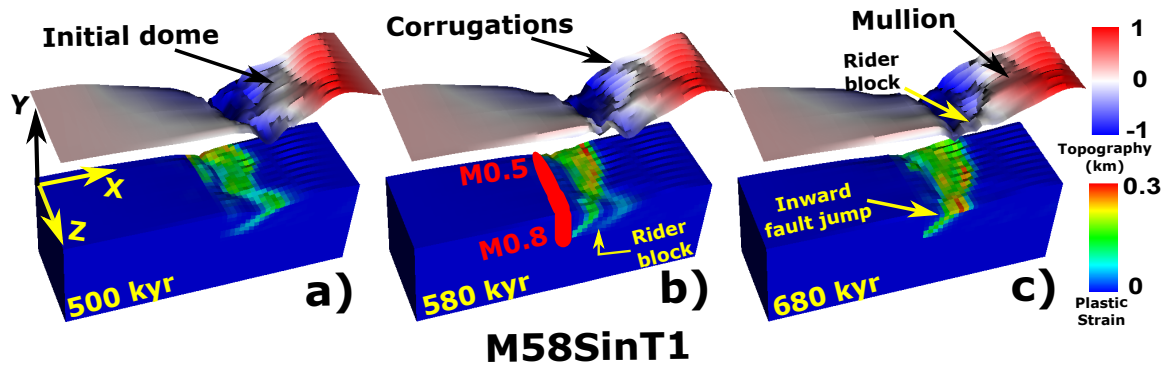


Figure 34: Evolution of faulting and morphologies of M58SinT1.

Between 530 kyr (Figure 32.e) and 550 kyr (Figure 32.f), another cut-back happens at

the lower M side ($0.5 < M < 0.545$) where a slump block with an area of $\sim 9 \text{ km}^2$ flows down the topography slope into the trough. Terminations recedes backward to the ridge axis. By 580 kyr, termination at the lower M side extends further away from the ridge axis due to less magma supply. Between 580 kyr and 850 kyr, due to two antithetic faults at the lower M side ($M \in (0.5, 0.53) \cup (0.56, 0.605)$), the termination at the lower M side recedes and the previous mirror reflected “S” shape termination evolves to a half circle curve (Figure 32.h). The shape is also reflected in the topography. By 960 kyr (Figure 32.i)), at the ridge segment with $M \in (0.62, 0.665)$, another inward fault jump replaces the detachment fault away from the ridge axis and retreats the termination backward to the ridge axis forming two half circle curves with wavelengths of around half of the model domain in z -axis. A large sinistral shear zone (red region $\sim 40^\circ$ oblique to ridge axis) is seen in the σ_{xz} panel. The shear stress σ_{xz} results from the inward fault jump at the center of the ridge segment that previous hanging wall changes to the footwall of the inward jumped fault and generates a offset between the old hangingwall at the lower M end and the new footwall of the inward jumped fault. By 1000 kyr, due to the along ridge coupling, the inward fault jump propagates to the higher M side (Figure 32.j).

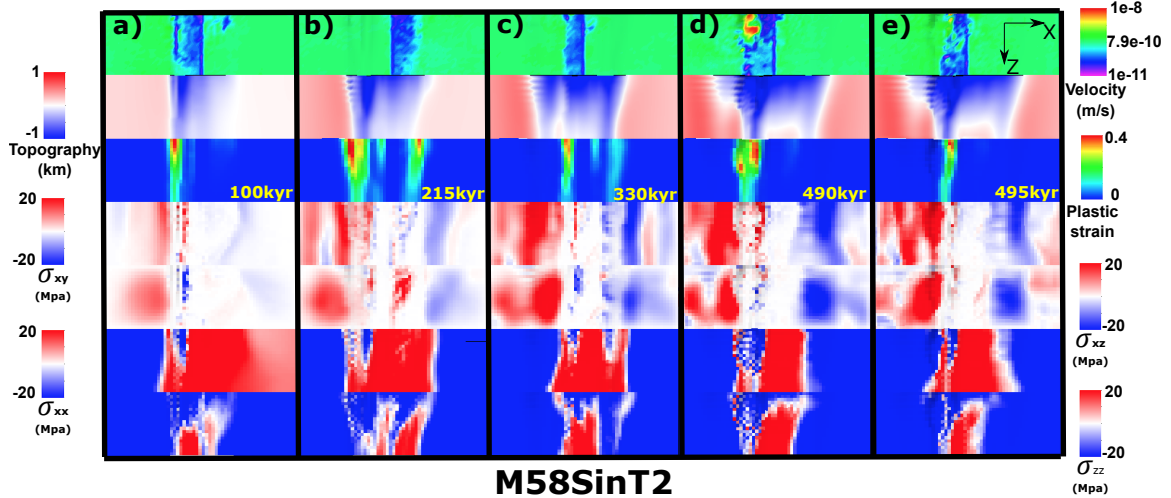


Figure 35: Faulting and stresses evolution of M58SinT2.

M58SinT2

As shown in Figure 35, a fault initiates on the left hand side of the ridge axis (Figure 35.a). The breakaway at the lower M side extends further than that of the higher M side. It takes longer time of ~ 100 kyr to form a localized fault plane through the whole ridge segment due to the slower rate of weakening (type 2). By 215 kyr (Figure 35.b), fault alternates to the conjugate plate and gradually replaces the initial one. Corrugations are only produced at the lower M side ($M \in (0.5, 0.62)$). By 330 kyr, fault alternates again. Between 490 kyr (Figure 35.d) and 495 kyr (Figure 35.e), a cut-back happens with mass wasting and termination receding. A slump block of an area of ~ 16 km² flows down the topography slope into the trough. With fault alternation, the shape of the median valley is no longer an hourglass. However, at the lower M side, the median valley is still wider and deeper. High frequency abyssal hills are produced at the higher M side. In addition, M58SinT2 has a fault alternation frequency of ~ 150 kyr which is higher than that of M88ConT2. ^{XT:}Reason for this difference needs further discussion.

3.4.3 M58SqrtT1 versus M58SqrtT2

The major difference between M58SqrtT1 and M58SqrtT2 is also whether the normal fault alternates or not.

M58SqrtT1

By 260 kyr, breakaway at $M = 0.5$ extends ~ 5 km further away from the ridge axis than that of the higher M end (Figure 36.a). Corrugations of a wavelength of ~ 2 km ^{XT:2}km is the correct wavelength for corrugations, change previous wrong ones of 1 km are produced along the ridge. By 370 kyr (Figure 36.b), due to larger value of $\frac{\partial M}{\partial Z}$ at the lower M side, a vertical tensile failure takes place at $M \in (0.5, 0.5949)$ ^{XT:}previous M range for Sin and Sqrt models should be revised, I used linear to calculate with respect to number of elements in Z. Start from this and the later ones are ok. Two parallel dextral shear stress zones (blue) are seen in the σ_{xz} panel. By 400 kyr (Figure 36.c), an inward fault

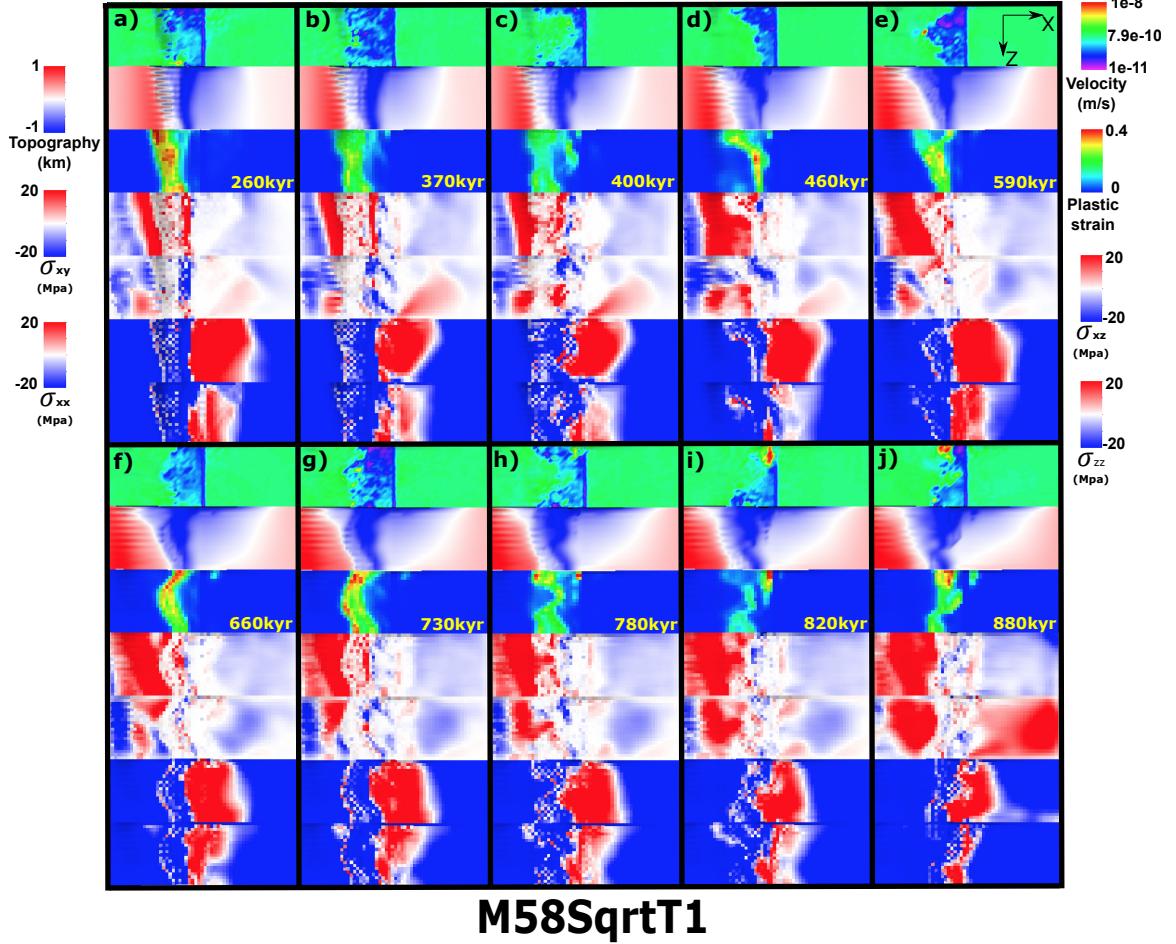


Figure 36: M58SqrtT1 (Table 2) faulting and stress evolution with respect to time.

jump happens at where $M \in (0.5949, 0.7121)$ and it propagates to the higher M end and replaces the initial detachment fault at the higher M side by 460 kyr (Figure 36.d). By 590 kyr (Figure 36.e), an inward fault jump happens at the lower M side ($M < 0.5949$) and connect with the normal fault at the higher M side replacing the initial detachment fault. An $\sim 18 \text{ km}^2$ triangular shape (bird's-eye view) rider block is produced at the lower M side. Termination at the center of the ridge segment extends furthest away from the ridge axis. This is because the previous inward fault jump first initiates there, so the fault starts slipping earlier and because the value of M is lower at the segment center than the higher M end. By 660 kyr (Figure 36.f), as the previous inward jumped fault at the higher M side evolves, another dome is produced. There is a hint of high angle normal fault at where

$M < 0.5949$ on the conjugate plate. But it doesn't develop. By 730 kyr (Figure 36.g, the termination evolves to a “half circle” and the shape is also seen in the topography. By 780 kyr (Figure 36.h), another inward fault jump appears at the ridge segment with $M \in (0.6342, 0.7121)$ and produced a curved termination with a wavelength of ~ 10 km. It has the potential to create a large wavelength mullion structure. Meanwhile, at the lower M side ($M < 0.5949$) near the ridge axis, an antithetic fault forms and propagates toward the higher M side (Figure 36.i). It triggers another inward fault jump to happen at the lower M side and produces another rider block. The inward jumped fault later connects with the detachment fault at the higher M side (Figure 36.j). In addition, a tensile failure shows its hint at the lower M side ($M < 0.6342$) of the conjugate plate.

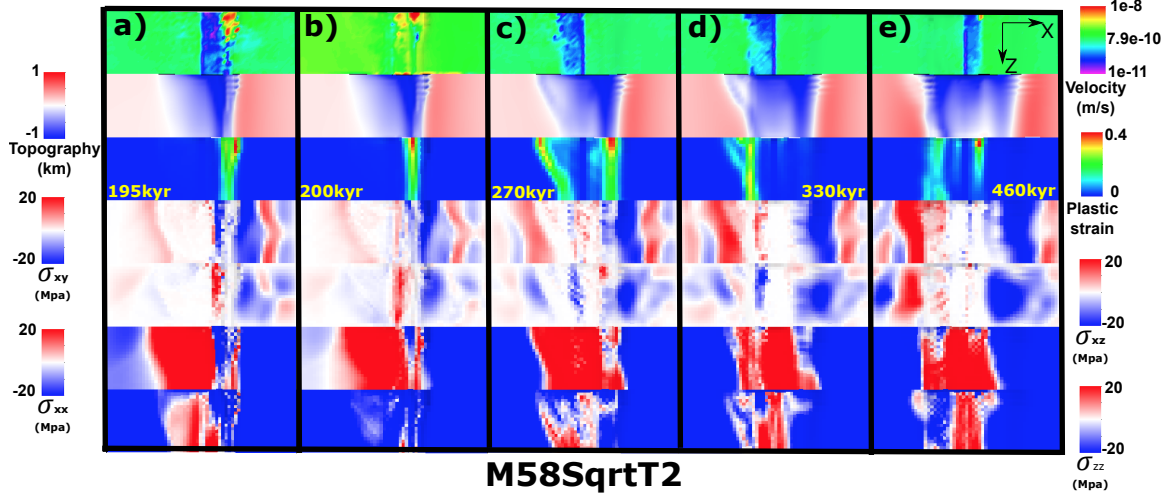


Figure 37: Faulting and stresses evolution for M58SqrtT2.

M58SqrtT2

By 195 kyr (Figure 37.a), breakaway at the lower M side extends further away from the ridge axis. Three corrugations begin to show up due to tensile failure. Median valley on the conjugate plate is wider at the lower M side because slow weakening allows a more distributed σ_{xx} that results in the elastic depression of the conjugate plate. Between 195 kyr (Figure 37.a) and 200 kyr (Figure 37.b), a cut-back happens with mass wasting along the ridge and is followed by the termination retreat. By 270 kyr fault al-

ternates (Figure 37.c). The shape of the alternated fault follows the curved shape shear σ_{xy} zone (red) as seen since ~ 195 kyr on the left hand side of the ridge axis. By 330 kyr (Figure 37.d), at the lower M side, an inward fault jump happens and takes the place of the old fault further away from the ridge axis. By 460 kyr (Figure 37.e), fault alternates again to the right hand side of the ridge axis.

3.5 Effects of the range of M variation

Generally, M57 and M58 models create a median valley much narrower and shallower than that of M28 models.

3.5.1 (M28 M57 M58)SinT1

M57SinT1 versus M58SinT1

For description of M57SinT1 evolution with respect to time, please refer to Section 3.4.1 and Figure 30. For description of M58SinT1 evolution with respect to time, please refer to Section 3.4.2 and Figure 32. Comparing M57SinT1 and M58SinT1, the major difference is that the faulting pattern evolution for M58SinT1 is much more dynamic with a higher frequency of inward fault jumps, cut-backs and connection of the offsetted fault zones. For M58SinT1, the inward fault jumps and antithetic faults usually replace the old ones. However, for M57SinT1, diking is not strong enough to create big enough stress perturbation along the ridge axis for inward fault jumps or antithetic faults to take the place of the original one. At the lower M side, antithetic faults only help to accommodate tensional stress which assists in maintaining a termination near the ridge axis while the termination at the higher M side gradually moves off axis. This produces an OCC with larger dome at the lower M side than that of higher M side which is opposite to the shape of the OCC produced by M58SinT1.

M28SinT1

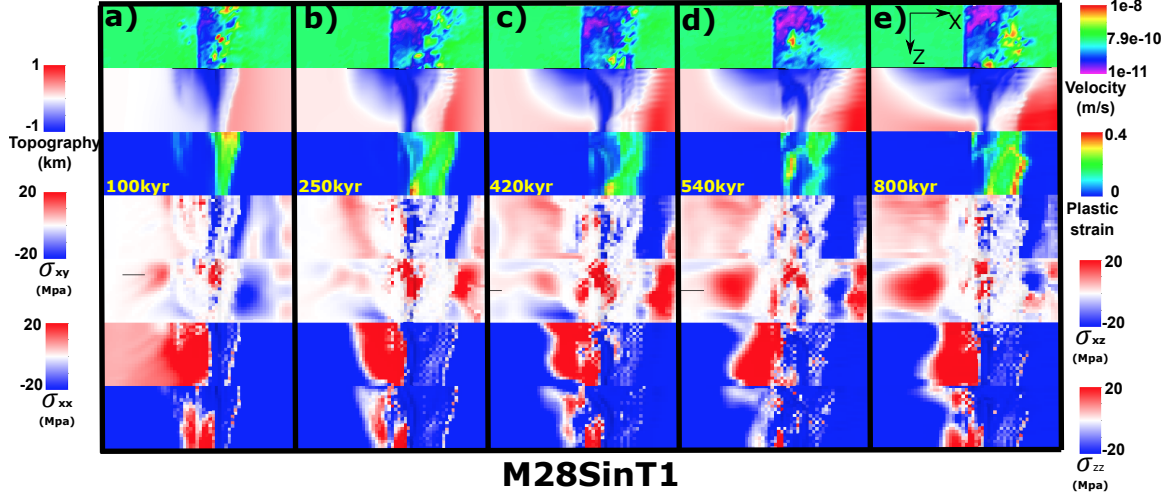


Figure 38: M28SinT1 (Table 2) faulting and stress evolution with respect to time.

As shown in Figure 38, faulting evolution is much less dynamic than that of M58SinT1. One detachment fault keeps active on the right hand side of the ridge axis. Only inward fault jump happens ~ 540 kyr (Figure 38.d). By ~ 100 kyr (Figure 38.a), breakaway at the lower M side extends ~ 4 km further away from ridge axis than the higher M side. By 250 kyr (Figure 38.b), ~ 4 corrugations begin to evolve at the lower M side ($M \in (0.2, 0.5135)$). By 420 kyr, at the higher M side, a hint of inward fault jump begins to show up. It develops into an inward fault jump by 540 kyr (Figure 38.d) and propagates toward higher M side. At the lower M side ($M \in (0.2, 0.2939)$), a tensile failure takes up part of the plate extension and helps maintain a closer to ridge axis termination than the extending termination at the region with $M \in (0.4724, 0.6562)$ (Figure 38.e). The curved in termination at the lower M side produces a mullion structure.

3.5.2 M57SinT2 versus M58SinT2

For description of M57SinT2 evolution with respect to time, please refer to Section 3.4.1 and Figure 31. For description of M58SinT1 evolution with respect to time, please refer to Section 3.4.2 and Figure 35. A major difference is that M57SinT2 has no fault alternation while M58SinT2 has.

3.5.3 M28LinT1 versus M57LinT1

For description of M28LinT1 evolution with respect to time, please refer to Section 3.1.

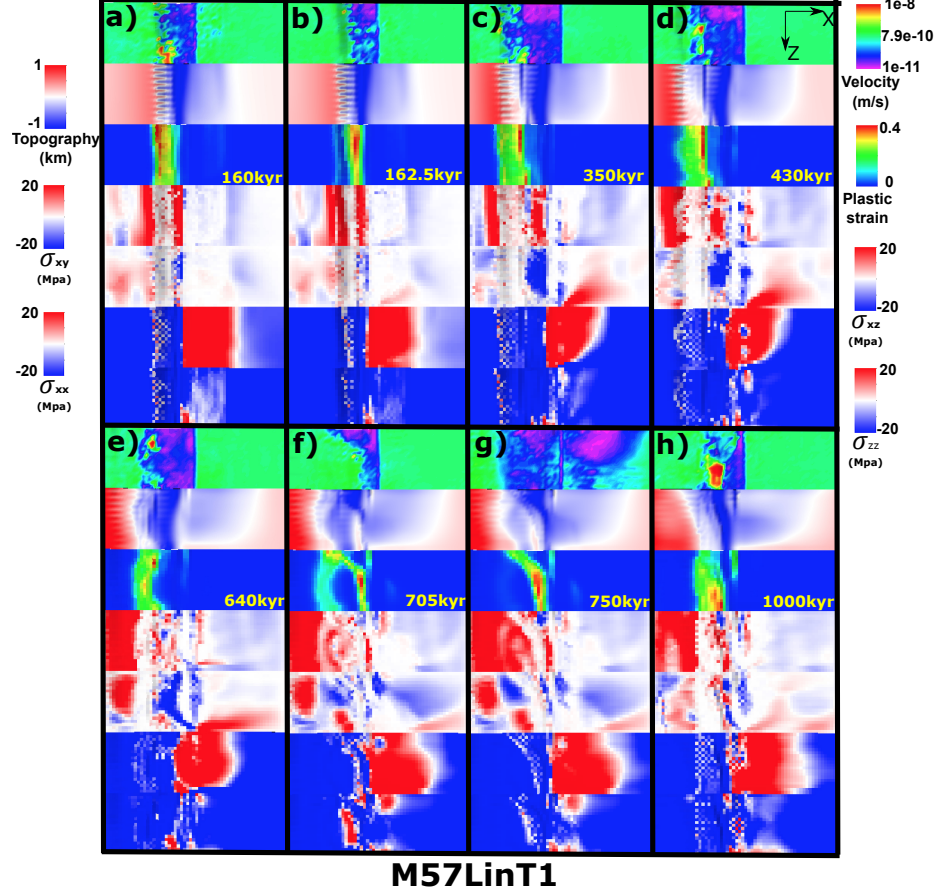


Figure 39: M57LinT1 (Table 2) faulting and stress evolution with respect to time.

M57LinT1

As shown in Figure 39, between 160 kyr (Figure 39.a) and 162.5 kyr (Figure 39.b), a cut-back happens. The corrugations have a relatively high amplitude. Due to less M variation (0.2), the along ridge offset in breakaways is smaller. The median valley almost has a constant width along the ridge. By 350 kyr (Figure 39.c), a tensile failure happens at the region with $M \in (0.5, 0.61)$ and generates a linear topography low. Another shorter tensile failure at the higher M side ($M > 0.64$) helps maintain a high angle normal fault near the ridge axis. By 430 kyr (Figure 39.d), the tensile failure at the lower M side ($M <$

0.52) is responsible for the retreat of the termination. While at where $M \in (0.54, 0.59)$, the termination extends further away from the ridge axis. This curved termination results in a “dog bone” shape topography as seen at 640 kyr (Figure 39.e) and is also responsible for the large dextral shear (blue) stress σ_{xz} . By 705 kyr (Figure 39.f), an inward fault jump happens and replaces the original detachment fault at the higher M side with a length of ~ 15 km. This inward jumped fault connects with the detachment fault at the lower M side. The new “L” shape termination is responsible for the topography seen at 1000 kyr (Figure 39.h). The termination at the higher M side soon catches up the further extended termination at the lower M side due to the presence of a tensile failure.

3.5.4 M28SqrtT1 versus M58SqrtT1

For description of the evolution of M28SqrtT1, please refer to Paragraph 3.2.5. For description of evolution of M58SqrtT1, please refer to Paragraph 3.4.3. Generally the faulting evolution for M58SqrtT1 is more dynamic with several inward fault jumps, antithetic faults, connection between offsetted faults along the ridge while M28SqrtT1 is simpler with only two cut-backs.

3.5.5 M57SqrtT2 versus M58SqrtT2

For description of evolutio of M58SqrtT2, please refer to Paragraph 2.

The major difference between M57SqrtT2 and M58SqrtT2 is that only M58SqrtT2 has fault alternation.

M57SqrtT2

For M57SqrtT2, six small scale cut-back happen at 282.5 kyr, 290 kyr, 365 kyr, 452.5 kyr, 482.5 kyr and 540 kyr respectively. As shown in Figure 40, the fault keeps on the left hand side of the ridge axis. By 200 kyr (Figure 40.b), an inward fault jump begins to evolve and takes the place of the initial fault. As the fault evolves, a stage of discon-

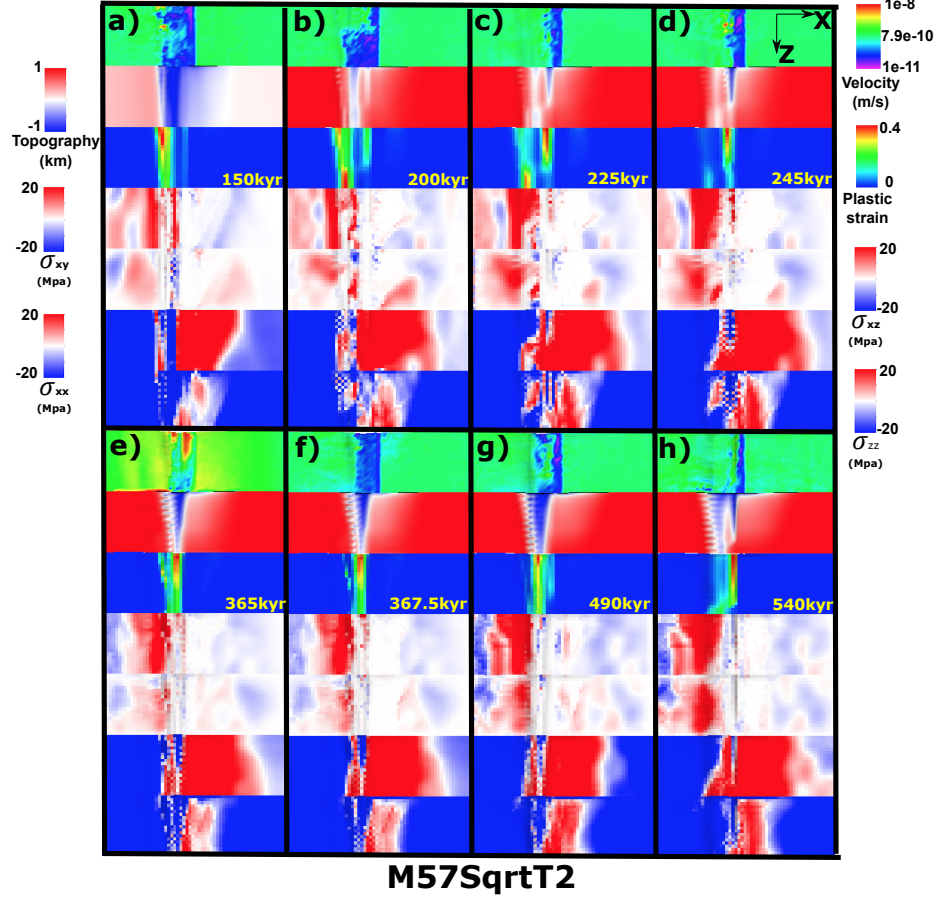


Figure 40: M57SqrtT2 (Table 2) faulting and stress evolution with respect to time.

tinuous abyssal hill is produced at the lower M side (Figure 40.c). The fault propagates toward the higher M side and cuts through the plate by ~ 245 kyr (Figure 40.d) when corrugations at the lower M side are produced. Between 365 kyr (Figure 40.e) and 367.5 kyr (Figure 40.f), a cut-back happens. By 490 kyr (Figure 40.g), an antithetic fault begins to evolve and terminates the old fault. It then develops into a vertical tensile failure at 540 kyr (Figure 40.h). *^{XT:} for M57SqrtT2, the topography since 200 kyr uplifted, I suspect there might be some runtime error for this model. Consider to abandon this model and if possible, rerun it.*

4 Discussion

4.1 Summary of Results

There are several behaviors that are controlled by the model parameters. Generally, only M58 models with type 2 weakening produce alternating faults on both side of the ridge axis. All the models show corrugations. As for faulting patterns in terms of evolution frequency, usually Square root is more dynamic than Sinusoidal than Linear, M58 is more dynamic than M57 than M28.

Following tables are a summery of the model behaviors with respect to different setup parameters.

Table 4: Model behaviors in short.

A	Alternating Fault	C	Corrugation	SL	Shear Topography Low
NA	Not Alternating	SF	Secondary Fault on one side	CB	Cut Back
DD	Double Dome	AM	Atlantis Massif Shape		

Based on the 11 models with M variation, we observed eight first-order behaviors as shown in Table 4.

Table 5: Linear functional form.

M range Type \\\diagdown	M28	M57	M58
Type one	NA; C; SL; SF _{1500 kyr} ; DD	NA; C; SF _{1380 kyr} ; CB _{330 kyr} ; AM(opposite z)	
Type two			

Generally, all models forms a median valley that deepens and widens toward the lower M side (Figure 8) except the reference model with constant M= 0.8 (Figure 13). The topography obseved in our models, to the first order, is controlled by the spatial and temporal distributions of faulting and to the second order, results from elastically deformation

Table 6: Sinusoidal functional form.

M range Type \	M28	M57	M58
Type one	NA; C; SL; SF _{995kyr}	NA; C; SL; SF _{760kyr;1320kyr} ; CB _{520kyr} ; AM	NA; C; SL; CB _{510kyr} ; SF _{760kyr;1140kyr;1990kyr}
Type two		NA; C; SL; SF _{680kyr} ; CB _{905kyr}	A _{450kyr;600kyr} ; C(only at low M); CB _{990kyr}

Table 7: Square root functional form.

M range Type \	M28	M57	M58
Type one	NA; C; SL; CB _{205kyr;330kyr;1025kyr}		NA; C _{1770kyr} (due to shear with dif wave length); SF _{860kyr} (high M); SF _{1190kyr} (low M)(Dog Bone); SF _{1690kyr}
Type two		NA; C; SF _{435kyr;1060kyr} ; CB _{585kyr} ; CB _{735kyr} ; CB _{910kyr} ; CB _{970kyr}	A _{550kyr;920kyr} ; C; CB _{400kyr}

(e.g. The gradual deepening and widening of the median valley; The bending of the crust at the footwall side of the detachment fault results in a domal shape of the fault interface as a mechanism for producing the dome shape of OCCs).

The pattern of the deformation (faulting and elastic deformation) is controlled by the evolving stress in the crust in terms of its distribution and magnitude. The stress evolution is a result of the interaction processes between tectonics and magmatism. Due to constant seafloor spreading, tensional stress orthogonal to the ridge-axis in the crust keeps accumulating. At the same time, along ridge-axis varying diking partially accommodates the stress from far field extension and perturbs the homogeneity state of stress distribution along the ridge-axis. Accumulated stress will be largely released when the tensile or shear failures establish.

Since the model behavior is very complicated. We will focus on the effects being

brought by the along ridge-axis variation in diking. Thus, it is worth considering a thought experiment with two end members: One, the along ridge-axis coupling is rigid, so that even along ridge axis variation in M exist, once a fault determined to develop, it will cut through the whole model domain along the ridge-axis(Z-axis) simultaneously. The other end member is that there is totally no coupling along the ridge-axis. So that each slice of crossection profile across the ridge behave separately without being influenced by its neighbour to a extreme that the model behavior is just a combination of 20 pseudo-2D models piled up along ridge-axis with their own M . (IMPORTANT: this suggests the importance and urgance for making clear conclusion and results description for previous pseudo-2D models results. However, one difficulty here is that the characteristic fault offset ΔX_c is different between 2D and 3D models.)

4.2 Fault Alteration

4.2.1 Trade-off between bending and weakening

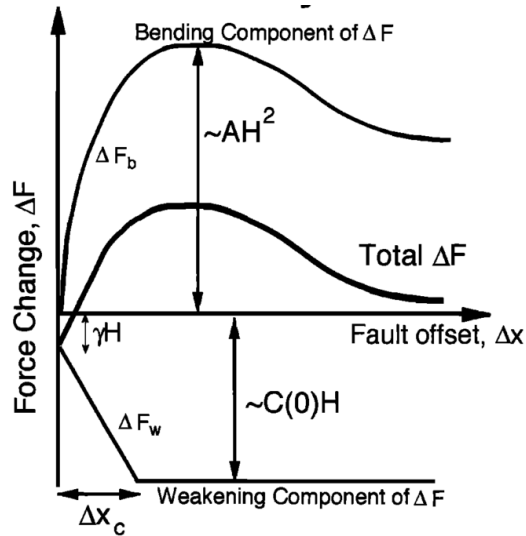


Figure 41: Trade-off between change in bending force ΔF_b and weakening in the fault interface ΔF_w . H is the thickness of the brittle crust and γ is the size of initial weak perturbation and A defines the maximum bending force change. (For more details, please refer to [Lavier et al., 2000])

Before we move on to each of the pairs, the framework studied by [Lavier et al., 2000] needs to be mentioned here for better understanding the model behaviors observed in our model results. There is a trade-off between change in bending force ΔF_b as a function of fault offset ΔX and force change ΔF_w as a function of ΔX due to strain weakening. As described in [Lavier et al., 2000], higher characteristic fault offset (ΔX_c) or slower strain weakening results in multiple faults rather than only one fault lasting. Whether conjugate fault and even multiple faults can be produced depends on the local stress condition. The strength weakening of the existed fault combines with how much bending force resists the fault to keep offsetting play a major role in determining the stress state at the other areas. As the sea-floor keeps spreading and ΔX increasing, the change in bending force ΔF_b increases and the strength at the fault interface decreases due to weakening ΔF_w (Figure 41). If the net force change $\Delta F = \Delta F_b + \Delta F_w$ is positive, it means that it is getting harder and harder to maintain the existing fault and stress will begin to accumulate at the other areas which eventually break another fault. ΔF_b initially increases fast with respect to ΔX and then when the breakaway bends over, it reaches its peak value and begins to decrease a little and maintains at a constant value. If the strain weakening is fast enough that the net effect force ΔF is always negative, then most of the stress will be released by the existing fault and thus no conjugate or multiple faults will be created.

Our model results verify this analysis that only Type two weakening (slower weakening with higher ΔX_c) can produce an alternating normal fault on the conjugate plate.

Based on the previous experience in pseudo-2D models and [Lavier et al., 2000], when $M > 0.5$, the frequency of normal faulting alternation is higher for higher characteristic fault offset (ΔX_c) of Type two weakening compared to Type one weakening. However, for the reference model two, M88ConT2 (Table 2), interesting enough, when comparing pseudo-2D and 3D models with Type two weakening under case of $M = 0.8$, even though the 3D Model has a larger ΔX_c of 1km than that of pseudo-2D model of 0.5km, the 3D model M88ConT2 has a lower frequency of faulting alternation. Since M

is constant 0.8 along the ridge-axis, the effect of along ridge coupling that resists alternation need not be considered. One possibility is that the resisting bending force increase in a higher rate than linear with respect to increasing the length of the ridge segment (Z_{max} km).

4.2.2 Alternating on conjugate plate

The fault alternation behavior observed in pseudo-2D models in cases $M > 0.5$ is much more complicated in 3D models. The results shows that only Type two weakening with M58 will result in a alternating faulting pattern. ^{XT:}integrate the area of $M > 0.5$ with respect to Z to see if there is any quantatative analysis available.

4.2.3 Secondary near-axis normal fault

The secondary near axis high angle normal fault is another common observation of the models. As shown in Figure 8, at the ridge axis with $M > 0.5$ (i.e. $Z > 10$), the existing normal fault will be pushed away from the ridge-axis due to excessive diking, as its mechanism has been mentioned in the introduction chapter, another new near axis normal fault is created at around 650kyr. As it evolve, the initial detachment fault become inactive (the transparent view of plastic strain shown in the rigth corner inset of time 880kyr). This secondary fault creates another dome and its composition is more likely to be volcanic rather than ultramafic, however, as is evolve, if it can last long, lower crust and upper mantle material can be exhumed to the surface. The composition of the domes observed at Kane magamullions is similar to this mechanism that ultramafic Babel dome is on the West and crustal inside-corner high on the East.

4.2.4 Effect of along ridge-axis coupling

The along ridge-axis coupling allowed the normal fault at the high M side ($M > 0.5$) to last for a long time and become a detachment that can produce a OCC. This behavior is

different from previous 2D studies that only $M=0.3 \sim 0.5$ can make OCCs and it also provides an alternative explanation for reconciling the gap between 2D model and observation described in [Olive et al., 2010]. Instead of magma injecting below brittle dutile transition, even injecting in the crust, due to along ridge coupling, model can still create OCC for high magma supply. Find the observation evidence for high M OCC from refs of Olive2010. As mentioned in the abstract of Olive2010, ref4-11 show a spectrum of magma supply.

4.3 Corrugations

There are two contributing factors, for one, trans-extenstional stresses are created due to offset of the breakaway as well as the variation in fault displacements along the ridge axis; for the other, the variation of the positions of the terminations of the detachment faults along the ridge-axis creates anastomosing faults that is mentioned in [Smith et al., 2014]. This anastomosing faulting behavior is largely responsible for corrugations in our models.

The stress at the tips of the breakaways is generally tensional in both parallel and orthogonal directions to the ridge-axis. (Figure ??f,g)

4.3.1 Wavelength of corrugations

4.4 Influence of healing

4.5 Comparing model results with nature observation

4.5.1 Cut back at 13°N Mid-Atlantic Ridge (M28SqrtT1)

The cut back behavior in M28SqrtT1 model creates a fault scarp of $\sim 1\text{km}$ in relief, 40km in length along the Z axis. Note that the fault scarp corresponds to initial formed break-away. The topography at 13°N Mid-Atlantic Ridge also has a fault scarp with very similar

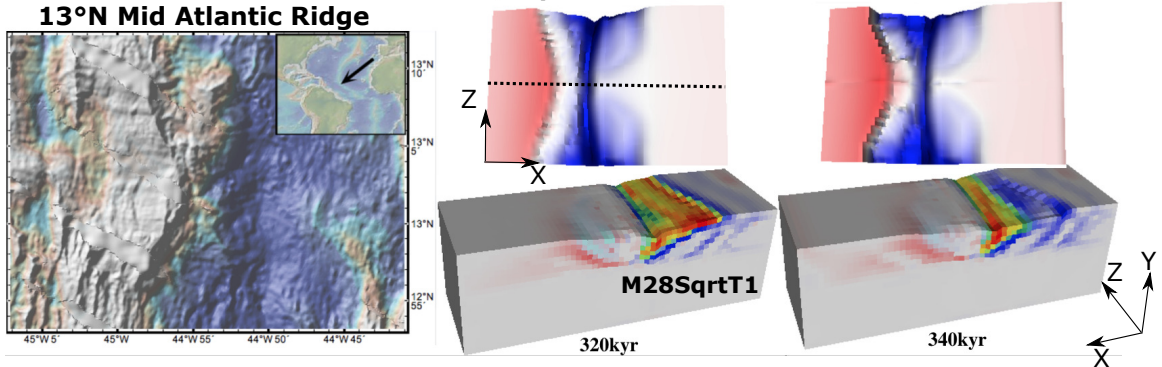


Figure 42: Comparing nature observation at 13°N Mid-Atlantic Ridge to the Cut back behavior of model M28SqrtT1. The model topography is a mirror symmetric flip according to the dash line, it reveals the case of M varies in a square root functional form from 0.2 to 0.8 to 0.2. For discussion on cut back formation mechanism, please refer to Section ???. The bathymetry is from GeoMapApp [Ryan et al., 2009].

geometry with $\sim 1\text{km}$ in relief. Due to the variation in diking along the ridge-axis, a sandglass shape of median valley is also produced in the model where the narrowest center corresponds to the region with high magma supply ($M=0.8$). This sandglass shape is also frequently observed in the nature along the Mid-Atlantic Ridges.

4.5.2 Double dome at 23°N Mid-Atlantic Ridge (Kane Megamullions) (Several models)

4.5.3 Atlantis Massif Shape at 30°N Mid-Atlantic Ridge ()

4.5.4 Shear low

4.5.5 Corrugations

4.6 Model Limitation

4.6.1 Fixed thermal structure effects and justification

Thermal conduction rate for $\kappa = 6\text{mm}^2/\text{s}$ material is $1.8\text{e}5 \text{ km/Myr}$, four magnitude faster compared to spreading rate of 2.5km/Myr .

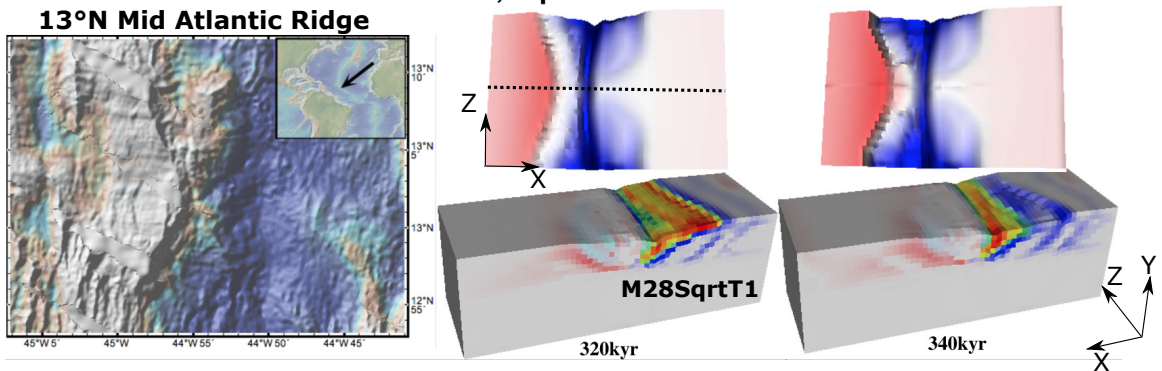


Figure 43: Comparing nature observation at 13°N Mid-Atlantic Ridge to the Cut back behavior of model M28SqrtT1. The model topography is a mirror symmetric flip according to the dash line, it reveals the case of M varies in a square root functional form from 0.2 to 0.8 to 0.2. For discussion on cut back formation mechanism, please refer to Section ??.

4.7 Recommendation for Future Research

5 Conclusions

Bibliography

- G. Baines, M. J. Cheadle, B. E. John, and J. J. Schwartz. The rate of oceanic detachment faulting at atlantis bank, sw indian ridge. *Earth and Planetary Science Letters*, 273(1-2):105–114, Aug. 2008. ISSN 0012821X. doi: 10.1016/j.epsl.2008.06.013.
- M. Behn, W. Buck, and I. Sacks. Topographic controls on dike injection in volcanic rift zones. *Earth and Planetary Science Letters*, 246(3-4):188–196, June 2006. doi: 10.1016/j.epsl.2006.04.005.
- M. D. Behn and G. Ito. Magmatic and tectonic extension at mid-ocean ridges: 1. controls on fault characteristics. *Geochemistry, Geophysics, Geosystems*, 9(8):n/a–n/a, Aug. 2008. ISSN 15252027. doi: 10.1029/2008GC001965.
- D. Blackman, J. Karson, and D. Kelley. Geology of the atlantis massif (mid-atlantic ridge, 30 n): Implications for the evolution of an ultramafic oceanic core complex. *Marine Geophysical ...*, 2002.
- D. K. Blackman, J. P. Canales, and A. Harding. Geophysical signatures of oceanic core complexes. *Geophysical Journal International*, 178(2):593–613, 2009. ISSN 0956540X. doi: 10.1111/j.1365-246X.2009.04184.x.
- R. Buck, L. Lavier, and A. Poliakov. Modes of faulting at mid-ocean ridges. *Nature*, 434(7034):719–23, 2005. ISSN 1476-4687. doi: 10.1038/nature03358.
- J. P. Canales, B. E. Tucholke, M. Xu, J. a. Collins, and D. L. DuBois. Seismic evidence for large-scale compositional heterogeneity of oceanic core complexes. *Geochemistry, Geophysics, Geosystems*, 9(8):n/a–n/a, Aug. 2008. ISSN 15252027. doi: 10.1029/2008GC002009.
- S. M. Carbotte, D. K. Smith, M. Cannat, and E. M. Klein. Tectonic and magmatic seg-

mentation of the global ocean ridge system : a synthesis of observations. *Geological Society of London*, 2015.

Y. J. Chen and J. Lin. Mechanisms for the formation of ridge-axis topography at slow-spreading ridges: A lithospheric-plate flexural model. *Geophysical Journal International*, 136:8–18, 1999. ISSN 0956540X. doi: 10.1046/j.1365-246X.1999.00716.x.

E. Choi, L. Lavier, and M. Gurnis. Thermomechanics of mid-ocean ridge segmentation. *Physics of the Earth and Planetary Interiors*, 171(1-4):374–386, Dec. 2008. ISSN 00319201. doi: 10.1016/j.pepi.2008.08.010.

A. Dannowski, I. Grevemeyer, C. R. Ranero, G. Ceuleneer, M. Maia, J. P. Morgan, and P. Gente. Seismic structure of an oceanic core complex at the mid-atlantic ridge, 22 ° 19'n. *Journal of Geophysical Research*, 115(B7):B07106, July 2010. ISSN 0148-0227. doi: 10.1029/2009JB006943.

H. J. B. Dick, M. a. Tivey, and B. E. Tucholke. Plutonic foundation of a slow-spreading ridge segment: Oceanic core complex at kane megamullion, 23 °30'n, 45 °20'w. *Geochemistry, Geophysics, Geosystems*, 9(5):n/a–n/a, May 2008. ISSN 15252027. doi: 10.1029/2007GC001645.

J. Escartín, D. K. Smith, J. Cann, H. Schouten, C. H. Langmuir, and S. Escrig. Central role of detachment faults in accretion of slow-spreading oceanic lithosphere. *Nature*, 455(7214):790–794, 2008. ISSN 0028-0836. doi: 10.1038/nature07333.

C. M. R. Fowler. *The solid earth: an introduction to global geophysics*. Cambridge University Press, 2004.

G. Ito and M. D. Behn. Magmatic and tectonic extension at mid-ocean ridges: 2. origin of axial morphology. *Geochemistry, Geophysics, Geosystems*, 9(9):n/a–n/a, Sept. 2008. ISSN 15252027. doi: 10.1029/2008GC001970. URL <http://doi.wiley.com/10.1029/2008GC001970>.

S. Kirby and A. K. Kronenberg. Rheology of the lithosphere: Selected topics. *Reviews of Geophysics*, 25(6):1219–1244, 1987.

L. L. Lavier, W. R. Buck, and A. N. B. Poliakov. Factors controlling normal fault offset in an ideal brittle layer. *Journal of Geophysical Research*, 105(B10):23431, 2000. doi: 10.1029/2000JB900108.

J. Lin, G. M. Purdy, H. Schouten, J.-C. Sempere, and C. Zervas. Evidence from gravity data for focused magmatic accretion along the Mid-Atlantic Ridge. *Nature*, 344:627–632, 1990. ISSN 0028-0836. doi: 10.1038/344627a0.

C. Mallows and R. C. Searle. A geophysical study of oceanic core complexes and surrounding terrain, mid-atlantic ridge 13 °n-14 °n. *Geochemistry, Geophysics, Geosystems*, 13(6):n/a–n/a, June 2012. ISSN 15252027. doi: 10.1029/2012GC004075.

J.-A. Olive, M. D. Behn, and B. E. Tucholke. The structure of oceanic core complexes controlled by the depth distribution of magma emplacement. *Nature Geoscience*, 3(7): 491–495, June 2010. ISSN 1752-0894. doi: 10.1038/ngeo888.

J.-a. Olive, M. D. Behn, and L. C. Malatesta. Modes of extensional faulting controlled by surface processes. *Geochemistry Geophysics Geosystems*, pages 1–9, 2014. doi: 10.1002/2014GL061507.

T. J. Reston and K. G. McDermott. Successive detachment faults and mantle unroofing at magma-poor rifted margins. *Geology*, 39(11):1071–1074, Oct. 2011. ISSN 0091-7613. doi: 10.1130/G32428.1.

T. J. Reston and C. R. Ranero. The 3-d geometry of detachment faulting at mid-ocean ridges. *Geochemistry, Geophysics, Geosystems*, 12(7):n/a–n/a, July 2011. ISSN 15252027. doi: 10.1029/2011GC003666.

- W. B. F. Ryan, S. M. Carbotte, J. O. Coplan, S. O'Hara, A. Melkonian, R. Arko, R. A. Weissel, V. Ferrini, A. Goodwillie, F. Nitsche, J. Bonczkowski, and R. Zemsky. Global multi-resolution topography synthesis. *Geochemistry, Geophysics, Geosystems*, 10, 2009. ISSN 15252027. doi: 10.1029/2008GC002332.
- H. Schouten, D. K. Smith, J. R. Cann, and J. Escartin. Tectonic versus magmatic extension in the presence of core complexes at slow-spreading ridges from a visualization of faulted seafloor topography. *Geology*, 38(7):615–618, June 2010. ISSN 0091-7613. doi: 10.1130/G30803.1.
- D. K. Smith, H. Schouten, H. J. B. Dick, J. R. Cann, V. Salters, H. R. Marschall, F. Ji, D. Yoerger, A. Sanfilippo, R. Parnell-turner, C. Palmiotto, A. Zhelezov, H. Bai, W. Junkin, B. Urann, S. Dick, M. Sulanowska, P. Lemmond, and S. Curry. Development and evolution of detachment faulting along 50 km of the mid-atlantic ridge near 16.5°n. *Geochemistry Geophysics Geosystems*, pages 4692–4711, 2014. doi: 10.1002/2014GC005563.Received.
- M. Tolstoy, A. J. Harding, and J. A. Orcutt. Crustal Thickness on the Mid-Atlantic Ridge: Bull's-Eye Gravity Anomalies and Focused Accretion. *Science*, 262(October):726–729, 1993. ISSN 0036-8075. doi: 10.1126/science.262.5134.726.
- B. E. Tucholke and J. Lin. A geological model for the structure of ridge segments in slow spreading ocean crust. *Journal of Geophysical Research*, 99(B6):11937, 1994. ISSN 0148-0227. doi: 10.1029/94JB00338.
- B. E. Tucholke, J. Lin, and M. C. Kleinrock. Megamullions and mullion structure defining oceanic metamorphic core complexes on the mid-atlantic ridge, 1998. ISSN 0148-0227.
- B. E. Tucholke, M. D. Behn, W. R. Buck, and J. Lin. Role of melt supply in oceanic de-

tachment faulting and formation of megamullions. *Geology*, 36(6):455, 2008. ISSN 0091-7613. doi: 10.1130/G24639A.1.

D. L. Turcotte and G. Schubert. *Geodynamics*. Cambridge, 2002.

D. L. Whitney, C. Teyssier, P. Rey, and W. R. Buck. Continental and oceanic core complexes. *Geological Society of America Bulletin*, 125(3-4):273–298, Dec. 2012. ISSN 0016-7606. doi: 10.1130/B30754.1.